12-10-2005

# Development Of Conjugate Heat Transfer Capability To An Unstructured Flow Solver - U2NCLE

Qingluan Xue

# DEVELOPMENT OF CONJUGATE HEAT TRANSFER CAPABILITY TO AN UNSTRUCTURED FLOW SOLVER - $U^2NCLE$

By

Qingluan Xue

A Thesis
Submitted to the Faculty of
Mississippi State University
in Partial Fulf llment of the Requirements
for the Degree of Master of Science
in Computational Engineering
in the College of Engineering

Mississippi State, Mississippi

December 2005

DEVELOPMENT OF CONJUGATE HEAT TRANSFER CAPABILITY TO AN UNSTRUCTURED FLOW SOLVER - $U^2NCLE$

By

Qingluan Xue

Approved:

| | |
|---|---|
| Chunhua Sheng<br>Associate Research Professor of Computational Engineering<br>(Major Professor) | Hyeona Lim<br>Assistant Professor of Mathematics and Statistics<br>(Committee Member) |
| Ioana Banicescu<br>Associate Professor of Computer Science and Engineering<br>(Committee Member) | Mark Janus<br>Associate Professor of Aerospace Engineering<br>(Graduate Coordinator of Computational Engineering) |

Roger King
Associate Dean of Research and Graduate Studies of the Bagley College of Engineering

Name: Qingluan Xue

Date of Degree: December 10, 2005

Institution: Mississippi State University

Major Field: Computational Engineering

Major Professor: Dr. Chunhua Sheng

Title of Study: DEVELOPMENT OF CONJUGATE HEAT TRANSFER CAPABILITY TO AN UNSTRUCTURED FLOW SOLVER - $U^2NCLE$

Pages in Study: 75

Candidate for Degree of Master of Science

A precise prediction of the heat loads in metal materials in contact with the hot gas is an increasingly demanding problem in the design phase of the complex cooling schemes in the modern turbine engines. The coupled calculation of the fluid flow and the heat transfer is a promising approach as heat transfer coefficients are not necessary in the calculation and the heat transfer itself is part of the calculation and can be derived from local heat fluxes. Therefore, it is useful to incorporate an appropriate scheme for directly coupled heat transfer computations (conjugate heat transfer), capable of handling complex geometries into the existing computational fluid dynamics (CFD) codes. The intent of the present work is to add the conjugate heat transfer solving capability to an existing flow solver.

The coupled approach is achieved by maintaining a continuous local heat flux and a common temperature at the points along the fluid-solid interface. At every iteration, the temperature which is directly calculated via the equality of the local heat fluxes passing

the fluid-solid contacting cell faces serves as the thermal boundary condition on the interfaces, instead of traditional isothermal/adiabatic thermal boundary conditions. In the solid domain, simplified energy equation is solved using the discretization and computational methods which have been used in the flow by introducing an effective equation of state. The connectivity is built for the points at the fluid-solid interfaces in order to communicate the thermal conditions with each other.

Validation of the developed conjugate capability has been investigated. Computed results have been compared with theoretical or experimental results for laminar flat plate, high pressure guide vane, cooled plate, and effusion-cooled plate. All results obtained thus far compare rather favorably with theoretical or experimental results.

# DEDICATION

To My Parents.

# ACKNOWLEDGMENTS

I would like to express my sincere gratitude to my major professor, Dr. Chunhua Sheng for his patient guidance and understanding throughout this endeavor. Also appreciation is expressed to the other members of my committee, Dr. Hyeona Lim, and Dr. Ioana Banicescu for their patience in look over this document. I greatly appreciate their help and insight though the class lectures and discussion.

Special thanks to Dr. Edward Luke and Dr. Mark Janus for their help.

I would like to thank for both their help and friendship include Dr. Wesley Brewer, Mithum Covilakom, Yang Zhang.

Finally, A heart felt thanks to my parents and the rest of my family who have always been supportive.

# TABLE OF CONTENTS

CHAPTER Page

# LIST OF TABLES

# LIST OF FIGURES

FIGURE Page

FIGURE Page

# LIST OF SYMBOLS, ABBREVIATIONS, AND NOMENCLATURE

| | |
|---|---|
| $i$, $j$, $k$ | unit vector in the Cartesian coordinate directions $x$, $y$, $z$ |
| $u$ | f ow velocity vector, $ui + vj + wk$ |
| $u$, $v$, $w$ | f ow velocity components in $x$, $y$, and $z$ directions |
| $c$ | grid velocity vector |
| $c_x$, $c_y$, $c_z$ | grid velocities in $x$, $y$, and $z$ directions |
| $n$ | unit normal vector associated with a control volume face |
| $e_t$ | total energy |
| $e_i$ | internal energy |
| $q$ | Cartesian primitive-variable vector, heat f ux |
| $q_x$, $q_y$, $q_z$ | heat f ux components in $x$, $y$, and $z$ directions |
| | Cartesian components of stress tensor |
| | viscosity |
| | second coeff cient of viscosity |
| $k$ | thermal conductivity |
| | ratio of specif c heat |
| $R$ | gas constant |
| | f uid density |
| $_s$ | solid density |

| | |
|---|---|
| $_{eff}$ | effective density |
| $p$ | pressure |
| $h$ | enthalpy |
| $Q$ | Cartesian conservative-variable vector |
| $F$ | f ux vector |
| $c_p$ | specif c heat (at constant pressure) |
| $c_v$ | specif c heat (at constant volume) |
| $L$ | length, lower-diagonal matrix |
| $_q$ | preconditioned matrix |
| $M$ | Mach number, transformation matrix, blowing ratio |
| $Re$ | Reynold number |
| $Pr$ | Prandtl number |
| $Pr_s$ | Prandtl number in solid |

Subscripts:

| | |
|---|---|
| $r$ | reference |
| | integration over control volume |
| | integration over control surface |
| $L$ | left side of a control volume interface |
| $R$ | right side of a control volume interface |
| $c$ | coolant |
| $m$ | main f ow |

# CHAPTER I

# INTRODUCTION

In several industrial applications it is becoming necessary to accompany the computation of the f ow and associated heat transfer in the f uid with the heat conduction within the adjacent solid. The coupling of these two models of heat transfer has been identif ed by the name “conjugate heat transfer” in the relevant literature. Typical applications where conjugate heat transfer effects can become important are, among others, the cooling of turbine blade and cooling of electronics. The continuous increase in turbine inlet pressure and temperature def nitely require reliable and accurate predictions of the main stream aerothermal characteristics and of the heat loads imposed to the blades so that a good design from a thermal point of view might allow a higher inlet temperature, less cooling air or a lighter design, thus increasing the performance or eff ciency of the turbine and resulting in a longer engine life. Another application is related to microelectronic cooling. During the past few years, the electronic industry has been demanding more and more eff cient heat exchanger design. In particular, the speed of electronic chips is seriously bounded by the thermal power that chips produce. A method to predict the heat loads in the design phase of a cooling scheme would be a very valuable engineering tool. It is therefore important to incorporate in existing computational f uid dynamics(CFD) codes

some appropriate scheme for coupled fluid flow and heat conductivity computations, capable of handing complex geometries. The intention of this work is directed towards adding the conjugate heat transfer solving capability into an existing flow solver.

Many flow solvers have been developed and widely used as good prediction tools for industrial design and analysis. They traditionally treat solid wall boundary condition as either an adiabatic wall condition (i.e zero heat flux across a solid wall) or an isothermal wall boundary conduction (i.e a constant temperature wall). When the working temperature distribution of a metal (like turbine blades, airfoils, microdevice) is computed, a conventional two-step uncoupled method has been developed : (1) treating two separate problem to determine both external and internal convective heat transfer coefficient; (2) passing these results as boundary condition to a finite element code and solving for conduction within the metal.

The current flow solver, referred to as $U^2NCLE$ (Unstructured UNsteady Computation of feLd Equations), is a scalable, parallel, implicit, viscous flow solver based on multi-element unstructured meshes developed at the Computational Simulation and Design Center of Mississippi State University. The flow solver only implements traditional adiabatic/isothermal thermal wall boundary conditions and does not address the coupling of heat conduction within solid bodies and convective heat in the fluid flow.

Today, conjugate heat transfer (Figure 1.1) is very popular and is a useful tool for thermal design and analysis in industrial applications. That is due to its advantages including simultanous calculation of the fluid/solid and no heat transfer distribution on the wall etc..

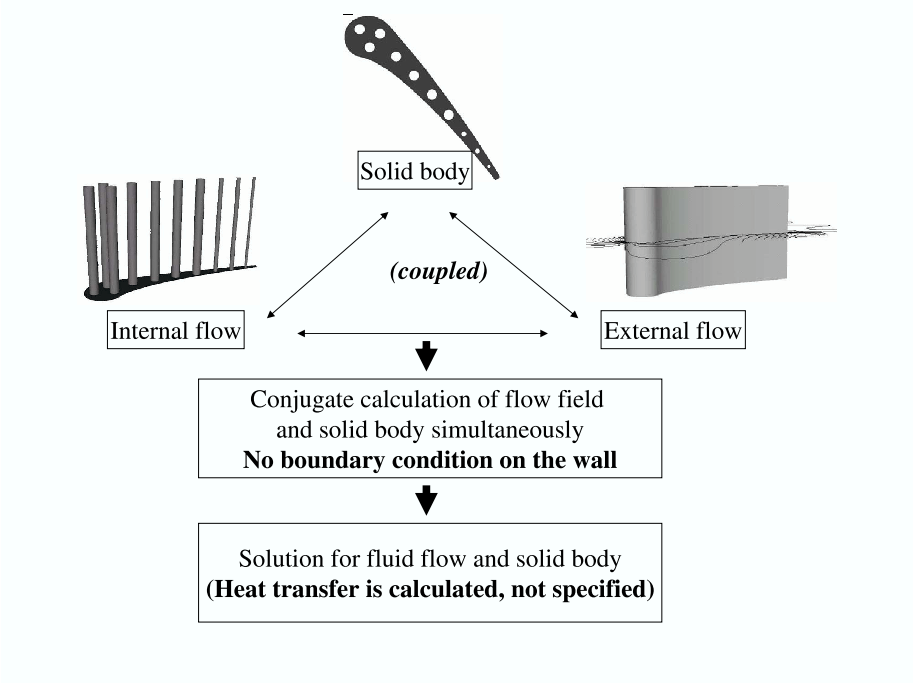


Figure 1.1 Schematic of the conjugate approach

Much research has been conducted to develop methods for the existing CFD codes to perform conjugate heat transfer by coupling a solid solver or by modifying the existing flow solver for solving the solid domain. Many applications have involved aerothermal analysis, like efficiency of different shapes of film cooling holes, impact of film cooling on the aerodynamic properties, design of film cooling holes, and design of microelectronics, etc. In the past few years, many papers in the technical literature have been published and show an increasing interest in the coupled method.

Kelkar et al. [1] have carried out conjugate transfer computations in boundary-fitted coordinates by using an "effective conductance" to define the interface conductivity between the solid and fluid regions. Papanicolaon et al. [2] have developed a procedure for

conjugate heat transfer calculations using a conservation-based discretization approach and applied it for the simulations in labyrinth and effusion cooled conbustor liners. Heidmann et al. [3] coupled the Glenn-HT code with a Boundary Element Method for solid. Based on the general multiblock Glenn-HT code, Rigby et al. [4] have proposed a coupled calculation procedure, which solves the simplif ed energy equation using the same method as in the gas region with minor changes to the numerical parameters. A numerical code with direct coupling of the f uid f ow and heat transfer computation has been developed and applied by Bohn et al.[5][6][7]. In their studies, the authors investigated the thermal barrier coating effect over an internally cooled blade [5], the inf uence of the more realistic conjugate heat transfer on the cooling air distribution, and secondary f ow etc. [6][7]. The research showed that the application of the conjugate method includes the inf uence of heat transfer on the velocity f eld within the cooling f lm. They also investigated the applicability of conjugate method on a realistic f lm-cooling conf guration of a modern gas turbine blade under hot gas operating conditions. York et al. [8] and Facchini et al. [9] have investigated a turbine vane cooled with air f owing radially through ten cooling holes. Both of them have assessed the impact of laminar-to-turbulent transition process on heat transfer behavior of the conjugate methodology. Culham et al. [10] incorporated a conjugate model to simulate microelectronic applications, and the comparison was made between the conjugate model and isolate heat source. Horvat et al. [11] have developed a computational algorithm based on the volume averaging technique to simulate conjugate heat transfer process in an electronic device heat sink. Han et al. [12] performed 2D and

3D conjugate heat transfer simulations of a hollow turbine vane with internal cooling cavities using an unstructured grid for fast turnaround. Montomoi et al. [13] have upgraded a CFD solver (HybFlow) to simulate heat transfer in gas turbine cooling device. Webster [14] has investigated the coupling of heating solver with a flow solver based on structured grid, and the coupling was achieved by passing the heat flux calculated on fluid-side interface to solid domain as a solid thermal boundary and returning a temperature to the fluid as fluid thermal boundary condition. Liu [15] has developed and implemented two heat transfer models and coupled them to a flow solver (CHEM). Also, the experimental activity conducted by Hylton [16] focused on measuring an accurate set of midspan data (pressure, solid temperature and HTC profiles) of a high pressure guide nozzle vane for code validation purpose.

The objective of the present study is to enhance the present flow solver by adding the conjugate heat transfer capability so that it can be as a useful tool for aerothermal design and analysis in turbomachinery and other related areas, as well as for aerodynamic simulations.

A part of the present work is directed at the development of the code for fluid-solid interface thermal communication. The goal is to couple the fluid flow and adjacent solid bodies by imposing the continuity of heat flux and temperature on the interface.

The general outline of the thesis is as following: The second chapter introduces the existing flow solver, which is the base of the present work. The third chapter discusses how heat-conduction can be solved using discretization and computational methods which

have been used in f ow domain in the solid bodies. This can be achieved by solving the simplif ed energy equation. The fourth chapter discusses the conjugate heat transfer procedure in the present work and the implementation of thermal communication between the interface. The f fth chapter presents the primary results of this work. All the results reported are for validation of the conjugate heat transfer solving ability developed in the existing code. Finally chapter six offers a summary and some conclusions stemming from this investigation.

# CHAPTER II

# INTRODUCTION TO THE FLOW SOLVER

This chapter is intended to outline the basic f ow solver ($U^2NCLE$). The present parallel, multi-element, unstructured, viscous f ow solver is based on domain decomposition for concurrent solution within subdomains, which are then assigned to multiple processors. The solution algorithm employs iterative solution of the implicit approximation, and its software implementation uses Message Passing Interface (MPI) for interprocessor communication.

## 2.1 Governing Equations

### *2.1.1 Navier-Stokes Equations*

The three-dimensional Reynolds-averaged Navier-Stokes equations for the time dependent, compressible, viscous f ow without body forces and external heat source have been written in integral form in Cartesian coordinate system as follows: mass conservation

$$\frac{}{t}\int dV + \oint \quad ( u \qquad c ) \quad ndA = 0 \tag{2.1}$$

momentum conservation

$$\frac{}{t}\int udV + \oint [\ u(\ u \quad c\ )\ \ n + n_x p \quad n_x\ _{xx} \quad n_y\ _{yx} \quad n_z\ _{zx}]dA = 0 \tag{2.2}$$

$$\frac{}{t}\int vdV + \oint [\ v(\ u \quad c\ )\ \ n + n_y p \quad n_x\ _{xy} \quad n_y\ _{yy} \quad n_z\ _{zy}]dA = 0 \tag{2.3}$$

$$\frac{}{t}\int wdV + \oint [\ w(\ u \quad c\ )\ \ n + n_z p \quad n_x\ _{xz} \quad n_y\ _{yz} \quad n_z\ _{zz}]dA = 0 \tag{2.4}$$

energy conservation

$$\frac{}{t}\int e_t dV + \oint [\ e_t(\ u \quad c\ )\ \ n + n_x(up \quad u\ _{xx} \quad v\ _{yx} \quad w\ _{zx} + q_x)$$

$$+n_y(vp \quad u\ _{xy} \quad v\ _{yy} \quad w\ _{zy} + q_y) + n_z(wp \quad u\ _{xz} \quad v\ _{yz} \quad w\ _{zz} + q_z)]dA = 0 \tag{2.5}$$

Here, $u$ and $c$ are the vectors of velocity and grid speed respectively, and are expressed as:

$$u = ui + vj + wk \qquad c = c_x i + c_y j + c_z k \tag{2.6}$$

The viscous stress components, under the assumption that the bulk viscosity is negligible ( $=$ $\frac{2}{3}$ ), are

$$_{xx} = \frac{2}{3}\ (2\frac{u}{x} \quad \frac{v}{y} \quad \frac{w}{z}) \tag{2.7}$$

$$_{yy} = \frac{2}{3}\ (2\frac{v}{y} \quad \frac{u}{x} \quad \frac{w}{z}) \tag{2.8}$$

$$_{zz} = \frac{2}{3}\ (2\frac{w}{z} \quad \frac{u}{x} \quad \frac{v}{y}) \tag{2.9}$$

$$_{xy} = \ _{yx} = \ (\frac{u}{y} + \frac{v}{x}) \tag{2.10}$$

$$_{xz} = \ _{zx} = \ (\frac{u}{z} + \frac{w}{x}) \tag{2.11}$$

$$_{yz} = \ _{zy} = \ (\frac{v}{z} + \frac{w}{y}) \tag{2.12}$$

The heat f ux terms are,

$$q_x = \ k\frac{T}{x} \qquad q_y = \ k\frac{T}{y} \qquad q_z = \ k\frac{T}{z} \tag{2.13}$$

where $k$ is the thermal conductivity, and $T$ is the temperature.

The system can be closed by two additional equations, the equations of state and the relation of pressure to internal energy. Assuming perfect gas, they are:

$$p = \ RT \tag{2.14}$$

$$e_i = \frac{p}{(\quad 1)} \tag{2.15}$$

where is the ratio of specif c heat for perfect gas, $R$ is the gas constant.

### *2.1.2 Vector Form of the Governing Equations*

A more convenient form of the Navier-Stokes equations used in numerical simulation is in vector form:

$$\frac{}{t}\int QdV + \oint \ F \ \ ndA = 0 \tag{2.16}$$

where $Q$ are conservative variables and $F$ is the f ux vector,

$$\mathbf{Q} = \begin{bmatrix} \\ u \\ v \\ w \\ e_t \end{bmatrix} \tag{2.17}$$

$$\mathbf{F}\ \ \hat{\mathbf{n}} = \begin{bmatrix} (u \quad c_x) & (v \quad c_y) & (w \quad c_z) \\ u(u \quad c_x) + p \quad {}_{xx} & u(v \quad c_y) \quad {}_{yx} & u(w \quad c_z) \quad {}_{zx} \\ v(v \quad c_y) \quad {}_{xy} & v(v \quad c_y) + p \quad {}_{yy} & v(w \quad c_z) \quad {}_{yz} \\ w(w \quad c_x) \quad {}_{xz} & w(w \quad c_y) \quad {}_{yz} & w(w \quad c_z) + p \quad {}_{zz} \\ e_t(u \quad c_x) \quad T_1 + q_x & e_t(v \quad c_y) \quad T_2 + q_y & e_t(w \quad c_z) \quad T_3 + q_z \end{bmatrix} \begin{bmatrix} n_x \\ \\ n_y \\ \\ n_z \end{bmatrix} \tag{2.18}$$

where,

$$T_1 = T_4 \quad up \qquad T_2 = T_5 \quad vp \qquad T_3 = T_6 \quad wp$$

$$T_4 = u\ {}_{xx} + v\ {}_{yx} + w\ {}_{zx} \quad T_5 = u\ {}_{xy} + v\ {}_{yy} + w\ {}_{zy} \quad T_6 = u\ {}_{xz} + v\ {}_{yz} + w\ {}_{zz}$$

### *2.1.3 Governing Equations with Preconditioning Matrix*

The present arbitrary Mach number code uses the preconditioning method by introducing a preconditioning matrix into the time derivative terms of the compressible governing equations [17]. The preconditioned governing equations are given by

$$M\ {}_q^{-1} \frac{}{t} \int q dV + \oint F\ \ n dA = 0 \tag{2.19}$$

where, ${}_q^{-1}$ is a constant diagonal matrix which depends on the reference Mach number $M_r$:

$${}_q^{-1} = diag[1\ \ 1\ \ 1\ \ 1\ \ \frac{1}{(M_r)}] \tag{2.20}$$

And $q$ is the primitive variables:

$$\mathbf{q} = \begin{bmatrix} \\ u \\ v \\ w \\ p \end{bmatrix} \tag{2.21}$$

$M$ is the transformation matrix from conservative $Q$ to primitive variables $q$:

$$\mathbf{M} = \begin{bmatrix} 1 & 0 & 0 & 0 & 0 \\ u & & 0 & 0 & 0 \\ v & 0 & & 0 & 0 \\ w & 0 & 0 & & 0 \\ \frac{|u|^2}{2} & u & v & w & \frac{1}{(\ -1)} \end{bmatrix} \tag{2.22}$$

### *2.1.4 Normalization of the Governing Equations*

Until now, the governing equations have been discussed in terms of dimensional variables. The normalization will be introduced in this section. This is especially important when there are large differences in magnitude in dimensional variables.

The dimensional variables (denoted by ) are nondimensionalized by the reference variables (denoted by $r$) with the following relations,

$$x = \frac{x}{L_r} \qquad y = \frac{y}{L_r} \qquad z = \frac{z}{L_r} \qquad u = \frac{u}{U_r} \qquad v = \frac{v}{U_r} \qquad w = \frac{w}{U_r}$$

$$= \frac{}{r} \qquad t = \frac{t}{T_r} \qquad p = \frac{p}{{}_r U_r^2} \qquad e = \frac{e}{C_p T_r} \qquad h = \frac{h}{C_p T_r} \qquad = \frac{}{r}$$

Usually, the reference variables are those of the free stream conditions. The non-dimensional governing equations of equation (2.19) are written in vector form as:

$$M \;\; {}_q^{-1} \frac{}{t} \int q dV + \oint \;\; F \;\; n dA = 0 \tag{2.23}$$

Where,

$$\mathbf{q} = \begin{bmatrix} \\ u \\ v \\ w \\ p \end{bmatrix} \tag{2.24}$$

$$\mathbf{F} \;\; \hat{\mathbf{n}} = \begin{bmatrix} (u \quad c_x) & (v \quad c_y) & (w \quad c_z) \\ u(u \quad c_x) + p \quad {}_{xx} & u(v \quad c_y) \quad {}_{yx} & u(w \quad c_z) \quad {}_{zx} \\ v(v \quad c_y) \quad {}_{xy} & v(v \quad c_y) + p \quad {}_{yy} & v(w \quad c_z) \quad {}_{yz} \\ w(w \quad c_x) \quad {}_{xz} & w(w \quad c_y) \quad {}_{yz} & w(w \quad c_z) + p \quad {}_{zz} \\ h_t(u \quad c_x) + T_1 + q_x & h_t(v \quad c_y) + T_2 + q_y & h_t(w \quad c_z) + T_3 + q_z \end{bmatrix} \begin{bmatrix} n_x \\ \\ n_y \\ \\ n_z \end{bmatrix} \tag{2.25}$$

Where,

$$T_1 = c_x E_c p \quad E_c T_4 \qquad T_2 = c_y E_c p \quad E_c T_5 \qquad T_3 = c_z E_c p \quad E_c T_6$$

$$T_4 = u_{\ xx} + v_{\ yx} + w_{\ zx} \quad T_5 = u_{\ xy} + v_{\ yy} + w_{\ zy} \quad T_6 = u_{\ xz} + v_{\ yz} + w_{\ zz}$$

The stress and heat f ux terms are,

$$_{xx} = \frac{}{Re}\frac{2}{3}(2\frac{u}{x} \quad \frac{v}{y} \quad \frac{w}{z}) \tag{2.26}$$

$$_{yy} = \frac{}{Re}\frac{2}{3}(2\frac{v}{y} \quad \frac{u}{x} \quad \frac{w}{z}) \tag{2.27}$$

$$_{zz} = \frac{}{Re}\frac{2}{3}(2\frac{w}{z} \quad \frac{u}{x} \quad \frac{v}{y}) \tag{2.28}$$

$$_{xy} = \ _{yx} = \frac{}{Re}(\frac{u}{y} + \frac{v}{x}) \tag{2.29}$$

$$_{xz} = \ _{zx} = \frac{}{Re}(\frac{u}{z} + \frac{w}{x}) \tag{2.30}$$

$$_{yz} = \ _{zy} = \frac{}{Re}(\frac{v}{z} + \frac{w}{y}) \tag{2.31}$$

$$q_x = \quad \frac{1}{Re}\frac{}{Pr}\frac{T}{x} \quad q_y = \quad \frac{1}{Re}\frac{}{Pr}\frac{T}{y} \quad q_z = \quad \frac{1}{Re}\frac{}{Pr}\frac{T}{z} \tag{2.32}$$

where $Re = \frac{_r U_r L_r}{_r}$ and $Pr = \frac{C_{p\ r}}{k}$. Finally, the non-dimensional equations of state to close the system are,

$$p = \frac{T}{M_r^2} \tag{2.33}$$

$$e_t = M_r^2[\frac{c^2}{} + \frac{(\quad 1)\ u^{\ 2}}{2}] \tag{2.34}$$

## 2.2 Numerical Scheme

Previously the governing equations of the physical problem were given. The numerical procedure to solve the governing equations will be described now. The solution technique is referred to as a node-centered, finite-volume, implicit scheme applied to general unstructured grid [17][18]. The governing equations are discretized using a finite volume technique, and the flow variables are stored in association with control volumes. The control volumes are formed by median duals which consist of connecting the centroid of each incident element to the midpoint of each incident edge. Surface integrals are approximated over the surface of the control volume [17][18].

### *2.2.1 Numerical Flux*

Preconditioned equations can be written in a different form as

$$M \ {}_q^{-1} \frac{q}{t} + \frac{}{x} F(q) = 0 \tag{2.35}$$

This can be expanded and rewritten as

$$M \ {}_q^{-1} \frac{q}{t} + M \ {}_q^{-1} a \ \frac{q}{x} = 0 \tag{2.36}$$

where $a$ is the system matrix for the preconditioned formulation. An eigensystem for $a$ is needed to develop characteristic-based flux approximations. $a = M^{-1}AM \ A =$

$F \quad Q$, and $M = \quad Q \quad q$. The flux approximation is evaluated using Roe's flux difference scheme with the arithmetic averaged variables $q = (\quad u \;\; v \;\; w \;\; h)$ [17][19].

$$= \frac{1}{2}(\;_L + \;_R) \tag{2.37}$$

$$u = \frac{1}{2}(u_L + u_R) \tag{2.38}$$

$$v = \frac{1}{2}(v_L + v_R) \tag{2.39}$$

$$w = \frac{1}{2}(w_L + w_R) \tag{2.40}$$

$$h = \frac{1}{2}(h_L + h_r) \tag{2.41}$$

Then the invscid flux approximation is

$$F_{i+1\ 2} = \frac{1}{2}(F_L + F_R) \quad \frac{1}{2}M\ ^{-1}_{q} \quad {}_q a \quad q \tag{2.42}$$

Here, $\quad q = q_R \quad q_L$ is the difference of the left and right state variables $q_L$ and $q_R$, across the faces of the control volumes. For first-order accurate differencing, $q_L$ and $q_R$ are set equal to the data at the nodes lying on either side of the face. For a high-order scheme, these variables are computed with a Taylor series expansion about the central node of the control volume.

The viscous terms can be discretized by a finite element or a finite volume technique. There are several methods used in the code, Galerkin finite element method [18], directional derivative method [18], and normal derivative method [17]. The normal derivative method is used in this work.

### *2.2.2 Iterative Procedures*

The numerical discretization of Equation (2.23) associated with the control volume surrounding vertex$0$ using the f nite volume approach on an unstructured grid is:

$$M \ {}_{q}^{-1} \frac{q^{n+1} \quad q_0^n}{t} + \frac{1}{V} \sum_{j \in N(0)} F_j \quad A_j = 0 \tag{2.43}$$

A nonlinear system of equations is generated from the above discretization, and Newton's method is used to linearize it [20]. In order to use Newton's method, f rst Equation (2.43) denoted as [17],

$$N(q_0) = M \ {}_{q}^{-1} \frac{q^{n+1} \quad q_0^n}{t} + \frac{1}{V} \sum_{j \in N(0)} F_j \quad A_j = 0 \tag{2.44}$$

Then a linear system of equations are obtained as,

$$N'(q_0^{n+1\,m})(q_0^{n+1\,m+1} \quad q_0^{n+1\,m}) = \quad N(q_0^{n+1\,m}) \tag{2.45}$$

The sequence of vector $q_0^{n+1\,m}$ converges to the solution vector $q_0^{n+1}$ where $n+1$ denotes the next time level.

The solution of the linear system of equations is obtained using an iterative method. In the present code, a symmetric implicit Gauss-Seidel method is used. A brief description of this method is given here. First, the system matrix is written as the sum of the diagonal ($D$), upper triangular ($U$), and lower triangular matrix ($L$):

$$A = D + U + L \tag{2.46}$$

where,

$$D = M \ {}_{q}^{-1} \frac{I}{t} + \frac{1}{V} \sum_{j \in N(0)} \frac{F_j}{q_{n+1}} \quad A_j \tag{2.47}$$

$$U = \frac{1}{V} \sum_{j \in N_U(0)} \frac{F_j}{q_{n+1}} \quad A_j \qquad L = \frac{1}{V} \sum_{j \in N_L(0)} \frac{F_j}{q_{n+1}} \quad A_j \tag{2.48}$$

Let $R^{n+1}$ be the vector of residual, and $q^{n+1}$ be the change of the variables. The symmetric Gauss-Seidel method can be written as the following two-step process per iteration [17][18]:

$$[L + D] \quad q^{n+1\ m+1\ k+\frac{1}{2}} + [U] \quad q^{n+1\ m+1\ k} = R^{n+1\ m} \tag{2.49}$$

$$[D + U] \quad q^{n+1\ m+1\ k+1} + [L] \quad q^{n+1\ m+1\ k+\frac{1}{2}} = R^{n+1\ m} \tag{2.50}$$

Where the $k$ denotes the symmetric Gause-Seidel iterative level. For the first pass, the solution sweeps forward through the vertices, and is saved into the buffer. For the second sweep, the same operations are performed, but loop backward through the vertices instead of forward.

## 2.3 Turbulence Model

A model for the effects of turbulence is a necessary component for simulating the high Reynolds number flows. In the present solver, the turbulence model is incorporated in a "loosely-coupled" procedure, that is, the mean flow equations are solved first and then the turbulence model is solved independently. Coupling between the two is accomplished since the turbulence model uses the most recently computed solution, and the solution of the core governing equations uses the most recently computed value of eddy viscosity [18]. The current solver has turbulence closure models: Spalart and Allmaras one-equation

turbulence model [21], and $k$ , $k$ , $q$ two-equation turbulence models [22]. The one-equation model is primarily used in this work.

## 2.4 Boundary Conditions

The boundary conditions of the f ow solver are characteristic variable boundary conditions (CVBC) [23]. The principle of these conditions is to determine the values of variables by way of the direction of the wave propagation, which may be into or out of the boundary. For the inf ow and outf ow, it is the Mach number that decides if the variables should be given or calculated using the inside variables. For no-slip solid wall conditions, the velocity of the f ow is zero relative to wall. In the current code, the thermal boundary conditions are limited to either adiabatic-wall condition or constant-temperature-wall condition. These thermal boundary conditions have been modif ed to include the condition of thermal coupling with the solid body (i.e., conjugate heat transfer), which will be discussed further in the following chapters.

# CHAPTER III

# HEAT CONDUCTION SOLVER IN SOLID DOMAIN

The objective of this work is to expand the present CFD flow solver capability by including the physical effect of the thermal conductivity in the solid regions. First, a modification is made to the code to solve the heat conduction in a solid region. It is achieved by setting a constant density and zero velocity in the solid domain, which results in a simplified energy equation. The simplified energy equation is equal to the heat conduction equations of solid part. Essentially all the discretization and computational methods which have been used in the flow domain were used in the solid domain. The details will be discussed in this chapter.

## 3.1 Governing Equation

### *3.1.1 Modified N-S Equations*

The physical process of heat conduction is described by the heat equation. The three-dimensional unsteady heat conduction equation without heat source has been written in integral form in Cartesian coordinates.

$$\frac{}{t}\int \quad {}_s c_p T dV + \oint \quad k\frac{T}{n}dA = 0 \tag{3.1}$$

Here $_s$ is the density of solid body, $c_p$ is the specif c heat, and $n$ is the outward unit vector of the control volume.

In the present work, the f ow solver will be modif ed to solve the heat equation. That is to say, the Navier-Stokes equations are also solved in the solid region. Hence, the following conditions are set: a constant density and zero velocity are used to satisfy the continuity and momentum equations, and energy equation is simplif ed to heat conduction equation. The resulting energy equations is

$$M\frac{}{t}\int pdV + \oint \quad F \quad ndA = 0 \tag{3.2}$$

Where $M = \frac{1}{-1}$, and $F$ is the f ux vector,

$$F \quad n = q_x n_x + q_y n_y + q_z n_z \tag{3.3}$$

The heat f ux terms are,

$$q_x = \quad k\frac{T}{x} \qquad q_y = \quad k\frac{T}{y} \qquad q_z = \quad k\frac{T}{z} \tag{3.4}$$

where $k$ is the thermal conductivity, and $T$ is the temperature.

Similarly, in the solid region, the system can be closed by the two additional equations, the “effective” equation of state and the relation of pressure to internal energy. They are:

$$p = \quad _{eff}RT \tag{3.5}$$

$$e_i = \frac{p}{_{eff}(\qquad 1)} \tag{3.6}$$

where $_{eff} = \frac{c_p}{c_v}$ $_s$ is the effective density, $p$ has no physical meaning and is used to close the equation, is the ratio of specif c heat for perfect gas, and $R$ is the gas constant.

### *3.1.2 Nondimensionalization*

The dimensional variables will be nondimensionalized by the reference variables which are used in the normalization of equations in the f ow region. The nondimensional governing equations of (3.2) are written in vector form as:

$$M\frac{}{t}\int pdV + \oint \quad F \quad ndA = 0 \tag{3.7}$$

$F$ is the f ux term,

$$F \quad n = q_x n_x + q_y n_y + q_z n_z \tag{3.8}$$

Where, the heat f ux terms are,

$$q_x = \quad \frac{1}{Re}\frac{}{Pr_s}\frac{T}{x} \qquad q_y = \quad \frac{1}{Re}\frac{}{Pr_s}\frac{T}{y} \qquad q_z = \quad \frac{1}{Re}\frac{}{Pr_s}\frac{T}{z} \tag{3.9}$$

where $Re = \frac{{}_r U_r L_r}{{}_r}$ and $Pr_s = \frac{C_{p\ \ eff}}{k}$. Here ${}_{eff}$ is the effective viscosity in the solid domain, which is a constant value. Finally, the nondimensional equations of state to close the system are,

$$p = \frac{T}{M_r^2} \tag{3.10}$$

$$e_t = e_i = M_r^2 \frac{c^2}{} \tag{3.11}$$

## 3.2 Numerical Scheme

To enhance the f ow solver to solve the temperature distribution in the solid domain, the modif ed Navier-Stokes equations are developed. The resulting simplif ed energy equation

is equal to Fourier equation. The same numerical methods are used in the solid region as in the f ow region. Since the density and velocity are constant in the solid region, the residual terms of continuity and momentum equations are set to zero in the numerical procedure.

### 3.3 Boundary Condition

The thermal boundary condition for solid region consists of constant temperature condition, zero heat f ux condition, and thermal coupling with f uid regions. The thermal coupling condition will be discussed further in the next chapter.

# CHAPTER IV

# COUPLING PROCEDURE OF INTERFACE

Until now the solver can solve the fluid flow in fluid field and the heat conduction in solid region. The purpose of this chapter is to discuss how to couple the physical effects of thermal energy transport between these two different regions.

## 4.1 Physical Procedure

The discussion is the criteria which can successfully achieve the physical interaction between the fluid and solid regions. The two physical conditions to be met are continuity of heat flux across the fluid-solid interface and a common temperature value on the interface. That is,

$$T_{fluid} = T_{solid} \tag{4.1}$$

$$k_{fluid}\frac{T}{n}_{fluid} = k_{solid}\frac{T}{n}_{solid} \tag{4.2}$$

The two conditions are imposed on each grid node along the interfaces as illustrated in Figure 4.1 and Figure 4.2. The following figures define a pair of interfaces (one is at the fluid boundary, the other is at the solid boundary)

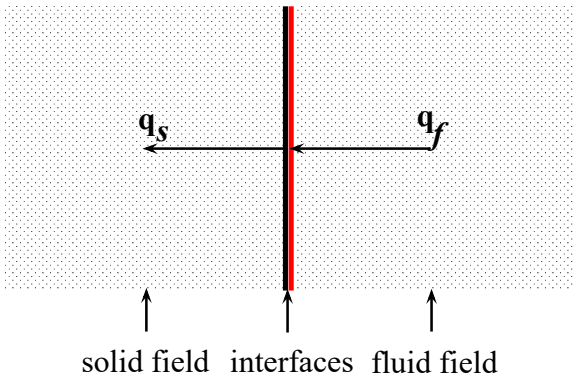


Figure 4.1 Continuity of heat f ux (top) at the f uid/solid interface

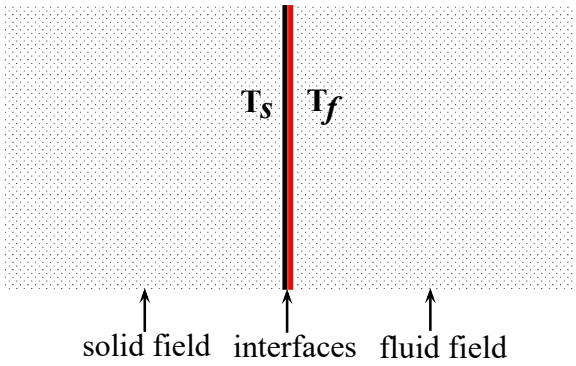


Figure 4.2 Continuity of temperature (bottom) at the f uid/solid interface

## 4.2 Procedure on Unstructured Grid

In the present work, the coupling of the fluid and solid fields is achieved by balancing the local heat fluxes at the contact interfaces on both fluid and solid sides. Thus a common wall temperature is produced at both sides at each iteration, which serves as an internal boundary condition for the coupling procedure. Similar approaches have been employed by several authors, such as Han et al. [12], Rigby and Lepicovsky [4]. Because the current work is based on unstructured, mixed-element grids (see Figure 4.3), evaluation of the local heat transfer flux based on the nodes on the interface is accomplished by an edge-weighted averaging procedure, as shown in Figure 4.3. For a specific node, one has the following formula,

$$\sum_{i=1}^{n} w_i k_f \frac{T_i \quad T_w}{n_i} = \sum_{j=1}^{m} w_j k_s \frac{T_w \quad T_j}{n_j} \tag{4.3}$$

Where indices $m$ and $n$ are the numbers of adjacent edges that connect to the interface nodes in the fluid and solid regions respectively. $i$ and $j$ are the indices of the edges connected to the nodes in the fluid and solid regions respectively. $w_i$ and $w_j$ are the associated edge weights, and $k_f$ and $k_s$ are the thermal conductivities of the fluid and solid respectively. $T_i$ and $T_j$ are the off-face node temperature adjacent to the interfaces. $T_w$ is the computed wall temperature at the interface node, which is used to provide a thermal boundary condition for both fluid and solid domain. During numerical procedure, the above equation is enforced iteratively at the fluid/solid interfaces.

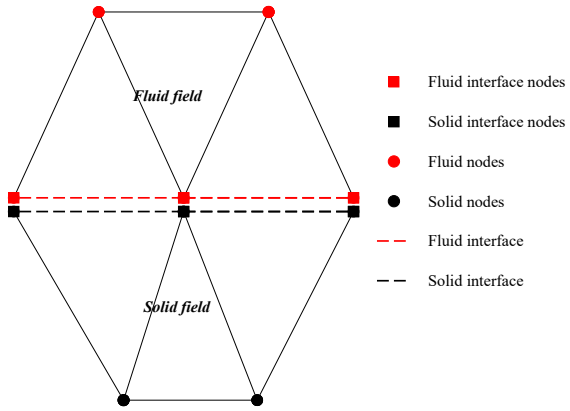


Figure 4.3 Schematic of the elements along the fluid/solid interface based on unstructured mesh ($2D$)

## 4.3 Implementation of Fluid-Solid Coupling

### *4.3.1 Solution Procedure*

For the conjugate implementation, modifications have been made. First, a solid volume tag was added to flag the solid computational domain. Fluid domains are treated in the normal way, with the exception that an additional boundary condition is added to handle fluid-solid interface. In the solid domains, the velocities are set to zero. The thermal conductivity was assumed constant for the present work.

At the fluid-solid interface, the velocities are zero and turbulence quantities on the fluid side are handled as they are normally at any other wall. The key issue here is setting the temperature. What essentially is required is to impose a condition at the boundary such that the temperature and heat flux match at the interface. When the above boundary condition is imposed, it is assumed that all values internal to each domain are known. It

is then possible to solve for the local wall temperature which will result in identical heat flux value from each side of the interfaces. Once the domain boundary values are set, the internal nodes are advanced. The procedure is repeated until convergence to steady state is achieved resulting in the matching of both temperature and heat flux at the fluid-solid interfaces.

### *4.3.2 Domain Topology along Interfaces*

The unstructured grid algorithm does not have the predictable connectivity of the structured grid, and all connectivities have to be built before they can be used. Figure 4.3 shows a pair of interfaces. Here, there are two assumptions: (1) there is no gap between interfaces, and (2) they are exactly matched at each node along the interfaces. Thus, the connectivity between the fluid interface and solid interface need to be built in order to perform the interaction between the fluid and solid domains in the computation.

### *4.3.3 Building the Connectivity between Interfaces*

To perform the coupling of fluid and solid domains, the message has to be passed and stored to either side of the interfaces in some way, since there is no connectivity between the fluid-solid interfaces. The idea here is that, in the preprocessing the identical mapping is built between the solid and fluid nodes on the interfaces. Based on the point-to-point match, it is to store the information of the neighbors of nodes on the fluid interface as the neighbors of the corresponding node on the solid interface, and to store the information of

the neighbors of nodes on the solid interface as the neighbors of the corresponding node on the fluid interface. The information includes the temperature and viscosity, which is updated at every iterative step.

### *4.3.4 Parallel Communication*

The present parallel unstructured viscous flow solver is based on a coarse-grained domain decomposition for concurrent solution within subdomains assigned to multiple processors. Explicit message passes are utilized for communication between processors, and each process has direct access to its local memory. So when information is updated at the fluid-solid interface at every iteration, the communication between processors has to be carried out explicitly.

The proposed information passing and communication hierarchy is shown in Figure 4.4. In the preprocessing, the point mapping between interfaces is made, and the initialized values of the temperature and the eddy viscosity are passed to each side of the interfaces. This work is done only once in the beginning of solution. In the local subdomain, the interface temperature is calculated and updated using passed temperature and eddy viscosity values. Then, the core governing equations are solved based on the thermal boundary conditions and the computed temperature will be communicated between subdomains to update the interface temperature at the next step. The turbulence model is solved using the recently computed solution, and the new eddy viscosity value will be communicated between the subdomains. Furthermore, the interface temperature will be

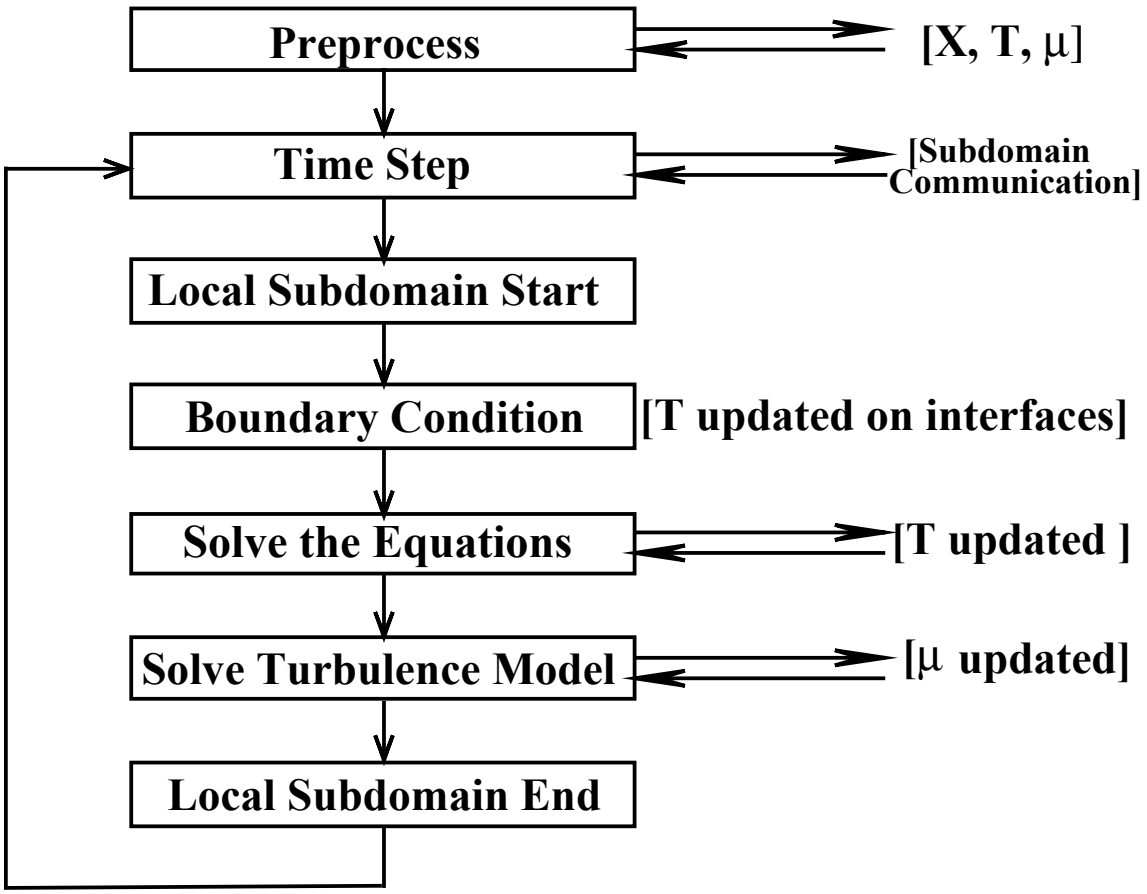


Figure 4.4 The solution procudure that incorporates the communication and information update along the interfaces

calculated using recently computed temperature and eddy viscosity values. This procedure is repeated at each time step until the solution converges.

# CHAPTER V

# VALIDATION AND RESULTS

The solid solving procedure and coupling procedure discussed in previous chapters are tested on several geometries. All grids are generated via the surface grid generator SolidMesh and the AFLR unstructured 3D grid generator. Results presented here include conduction heat transfer inside a metal flat plate, flow field over a flat plate, a turbine nozzle guide vane with ten radially cooled holes, a cooled flat plate, and an effusion-cooled plate.

## 5.1 Validation of the Heat Conduction in the Solid Domain

The heat conduction solving capability is added to the flow solver by some modifications discussed in Chapter 3. Here one relatively simple test case on a three-dimensional grid will be used to demonstrate that the heat conduction capability works properly. The test case assumes constant thermo-physical properties, which gives a linear heat equation. Also, the test has an analytical solution against which comparisons can be made.

This case is that of a one-dimensional, steady conduction problem. It is sometimes referred to as conduction through an "infinite slab", the strictly necessary physical situation

[24]. For the “inf nite slab” physical model, Fourier’s law is simplif ed to one-dimensional Laplace’s equation.

$$\frac{d^2T}{dx^2} = 0 \tag{5.1}$$

Which integrates to

$$T = Bx + C \tag{5.2}$$

With boundary conditions $T = T_1$ at $x = x_1$ , and $T = T_2$ at $x = x_2$ , so that

$$T = \frac{T_2 \quad T_1}{x_2 \quad x_1} x + C \tag{5.3}$$

To simulate the “inf nite slab”, the model of f nite length has a length to thickness ratio of $10$ as depicted in Figure 5.1.

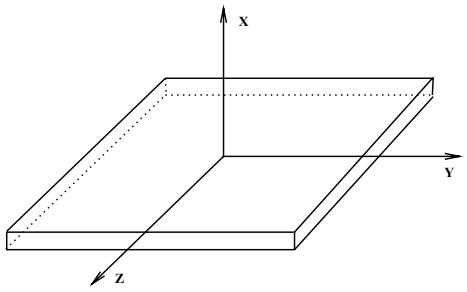


Figure 5.1 Computational domain of the inf nite slab

The specif cations of the physical length, conductivity, density, and specif c heat of the model are in the following Table:

Table 5.1 Parameters of Slab

| length | conductivity | specif c heat | density |
|---|---|---|---|
| X=0.1m Y=Z=1.0m | 17.0 W/(m-K) | 568 J/(Kg-K) | 8900 Kg/m |

The thermal boundary conditions are: (1) $300K$ and $600K$ are specif ed on the $x = 0\ 0$ and $x = 0\ 1m$ faces respectively; (2) all other faces are treated as adiabatic wall boundary conditions.

A plot of the numerical and analytical temperature prof les along the $x$ direction is given in Figure 5.2, which shows that they are in very good agreement. Here, the temperature and $x$ are normalized by $300K$ and $0\ 1m$ respectively. Figure 5.3 shows the temperature contours of the plate. The contour lines are parallel along the $x$ direction, except at both the ends having the adiabatic boundary conditions. It demonstrates the linear heat property.

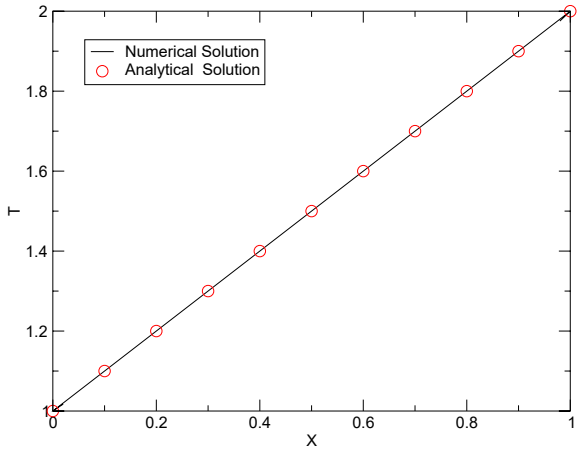


Figure 5.2 Temperature prof le along the streamwise direction ($x$)

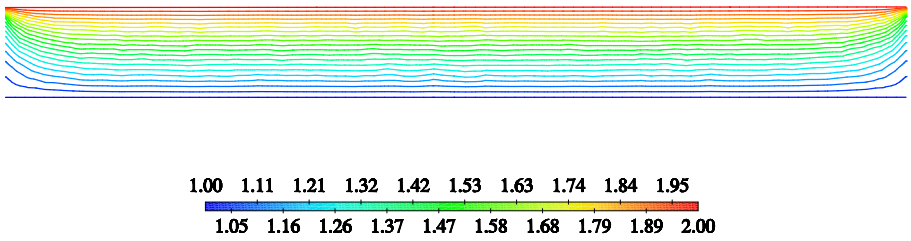


Figure 5.3 Temperature contour plot along the streamwise direction ($x$)

## 5.2 Validation of Fluid-Solid Coupling

### *5.2.1 Flow f eld over a Flat Plate*

This test case is the laminar f ow over a f at plate with conjugate heat transfer between the f uid and the metal plate itself, for which several analytical solutions are available. A laminar case has been chosen intentionally to decouple the validation of the scheme from the effect of turbulence models.

#### 5.2.1.1 Boundary Conditions

The air f ow presents a static temperature of $T = 460K$, a Mach number equal to $0\ 13$ and a uniform velocity as inlet conditions. Cooling is guaranteed to the plate from

the lower surface, where uniform wall temperature is imposed ($198K$). No explicit temperature is given for upper surface, while the thermal condition is calculated using the fully-coupled approach at every iteration. The plate thickness for the model used is $5mm$ and the thermal conductivity is $k = 17\ 0w\ \ mK$.

#### 5.2.1.2 Results and Analysis

A comparison between the CFD results and the analytical solution given by Luikov [25] has been performed. Luikov estimated the temperature prof le normal to wall in both f uid and solid f eld and Nusselt numbers in the f uid f eld. The dimensionless temperature ( ) prof les are reported below (Figure 5.4 and Figure 5.5). The dimensionless temperature is def ned as

$$= \frac{T \quad T_b}{T_\infty \quad T_b} \tag{5.4}$$

The agreement between the analytical solution and numerical calculation is satisfactory as shown in the f gures(Figure 5.4 and Figure 5.5). One temperature prof le is located at $x = 1mm$ (see Figure 5.4), while the other is located at $x = 10mm$ (see Figure 5.5). However, it was observed that a small discrepancy appears for $x$ values very close to the plate leading edge. While proceeding further downstream the agreement between analytical solution and calculation is quite high. Concerning Figure 5.4, it is suggested that the developing boundary layer in the neighborhood of the plate leading edge is somewhat delayed normal to the wall.

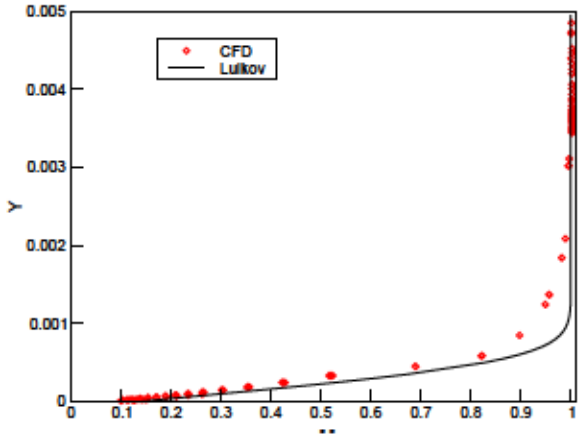


Figure 5.4 Temperature distribution prof le in the normal direction ($y$) at $x = 1mm$

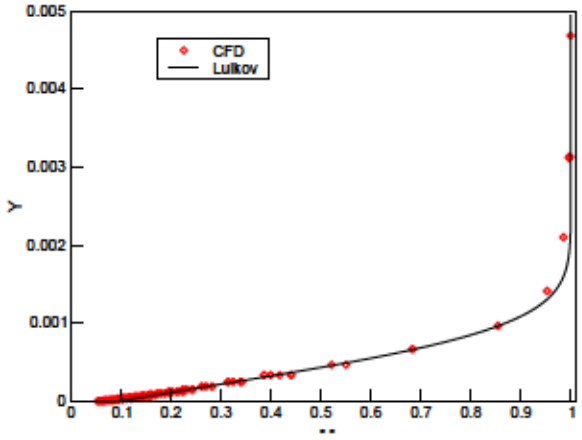


Figure 5.5 Temperature distribution prof le in the normal diration ($y$) at $x = 10mm$

Heat transfer results are presented in terms of Nusselt number ($Nu_x$) and heat coeff cient ($H$) on the upper plate surface. The Nusselt number and heat coeff cient are respectively def ned as

$$Nu_x = \frac{Hx}{k} \tag{5.5}$$

$$H = \frac{q_w}{T_w \quad T_a} \tag{5.6}$$

Where $q_w$ is the heat f ux at the wall surface. $T_w$ is the wall temperature, and $T_a$ is the inlet temperature. $H$ and $k$ are heat coeff cient and conductivity respectively.

Figure 5.6 is a plot of the Nusselt Number along the stream-wise direction ($x$), and Figure 5.7 is a plot of the heat coeff cient along the stream-wise direction. The red curves are the theoretical solutions given by Luikov. The black curves are the coupled solutions. It is found that reasonable agreement has been achieved.

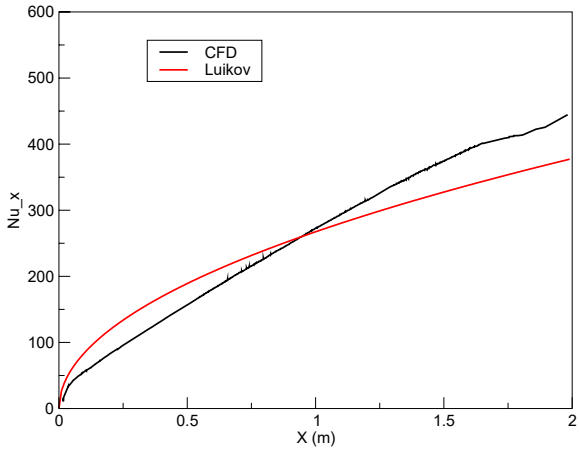


Figure 5.6 Nusselt number distribution curves in the streamwise direction ($x$)

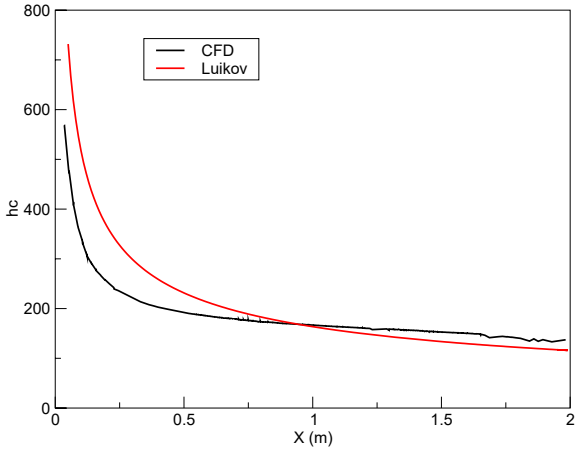


Figure 5.7 Heat transfer coeff cient distribution curves in the streamwise direction ($x$)

### *5.2.2 High Pressure Turbine nozzle guide Vane*

#### 5.2.2.1 Test Vane Geometry

The conf guration considered is that of a high pressure turbine nozzle guide vane (MarkII), which is convectively cooled by ten radial channels supplied with air. The cross-sectional view of the vane with hole conf gurations is shown in Figure 5.8. It is a linear vane with height of $3\ 983cm$, and its chord length is $13\ 622cm$. The vane is with setting angle of $63\ 69$ degrees and air exit angle of $70\ 96$ degrees. The diameter of the holes are shown in Table 5.3 . Hylton et al. [16] had conducted extensive experiments on the vane under near engine operating conditions. The vane is made of ASTM type 310 stainless steel, which has a constant density of $7900kg\ \ m^3$ and a specif c heat of $586\ 5J\ \ (kg\ \ \ k)$ over the range of temperatures in the present problem. The thermal conductivity varies with temperature;

but the constant value of $17\ 0W\ (mk)$ based on the avarage temperature is used in current computations.

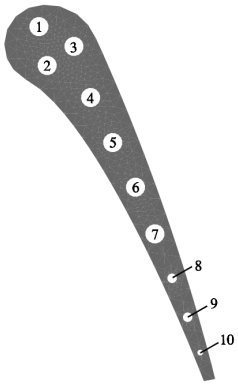


Figure 5.8 Cross-sectional view of the geometry of the nozzle guide vane

5.2.2.2 Computational Domain, Grid and Boundary Conditions

A view of the computational domain is shown in Figure 5.9. The left and right surface are the inlet and outlet respectively. The inlet of the passage is located one chord length upstream of the blade leading edge, and the exit is located two chord lengths from the trailing edge. The upper and lower surfaces of the boundary are peroidic surfaces. Periodic conditions were employed to duplicate the multiple vane passages in the experiment, and therefore only one passage is computed in the simulation. The center is the vane with cooling holes. Note that the top and bottom end (transparent) boundaries are solid walls. The grid of one passage channel has approximately $4\ 0$ million points. A view of the com-

putational grid on the cross-section planes is given in Figure 5.10 and Figure 5.11. At the f uid-solid interfaces a high resolution grid in the normal direction was generated to maintain the accuracy of temperature calculation. The thermal condition on the vane external surface is determined by the fully coupled conjugate approach. The thermal boundary on each internal cooling channel is explicitly specif ed temperature values based on experimental data [16]. Table 5.3 lists the temperatures of each cooling hole used in both simulations. The hub and tip walls are moduled with no-slip and adiabatic conditions. Two cases, one with a subsonic exit Mach number (Case 1) and the other with a supersonic exit Mach number (Case 2), are simulated with the same inlet and outlet conditions as reported in the experiment. Hylton [16] et al. reported an average Mach number at a pressure rank located just aft of the blade trailing edge plane at the midspan. An average static back pressure is determined based on the Mach number and the isentropic f ow relations. This experimental condition of average pressure was achieved in the simulation by adjusting the back pressure further downstream at the exit of the computational domain. The f ow operating conditions for both subsonic and supsonic exit Mach number cases are listed in Table5.2. A constant specif c ratio of 1 3 was used in the calculations. The Reynolds numbers are based on the chord length and the inf ow velocity and temperature.

Table 5.2 Operating Conditions in the Simulations

| $Case$ | $Re$ ( $10^6$) | $P_0$ ($bar$) | $T_0$ ($K$) | $P_e$ ($bar$) | $M_{in}$ | $Mex$ |
|---|---|---|---|---|---|---|
| 1 | 0 57 | 3 38 | 811 | 1 78 | 0 18 | 0 90 |
| 2 | 0 56 | 3 32 | 811 | 1 74 | 0 19 | 1 04 |

Table 5.3 Cooling Channel Diameter and Temperatures ($K$)

| $Holes$ | $Diameter(cm)$ | $Case1(K)$ | $Case2(K)$ |
|---|---|---|---|
| 1 | 0.63 | 449.6 | 435.9 |
| 2 | 0.63 | 449.6 | 442.5 |
| 3 | 0.63 | 438.5 | 406.8 |
| 4 | 0.63 | 425.7 | 411.9 |
| 5 | 0.63 | 456.3 | 450.5 |
| 6 | 0.63 | 459.6 | 455.5 |
| 7 | 0.63 | 467.4 | 469.4 |
| 8 | 0.31 | 490.7 | 496.8 |
| 9 | 0.31 | 529.7 | 535.9 |
| 10 | 0.198 | 545.3 | 547.7 |

#### 5.2.2.3 Results and Analysis

The results of the simulations are presented and analyzed here. For both operating conditions (Case 1 and Case 2), the flow field aerodynamic loading is examined first, followed by the temperature field and heat transfer distribution. Three two-equation turbulence models are also used besides the Spalart-Allmaras turbulence model. First, the analysis is based on the Spalart-Allmaras model, and then the comparison between all turbulence models is given. All results are compared with the experimental data from the work of Hylton et al. [16]. All the plots are located at the vane midspan plane.

Subsonic Case:

The predicted aerodynamic loading for Case 1 in the form of pressure distribution at the vane midspan is given in Figure 5.12, along with the experimental data. The predictions

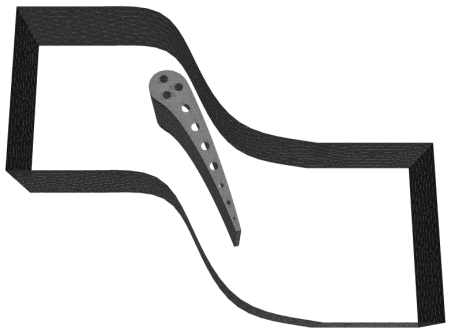

Figure 5.9 Diagram of the computational domain for nozzle guide vane

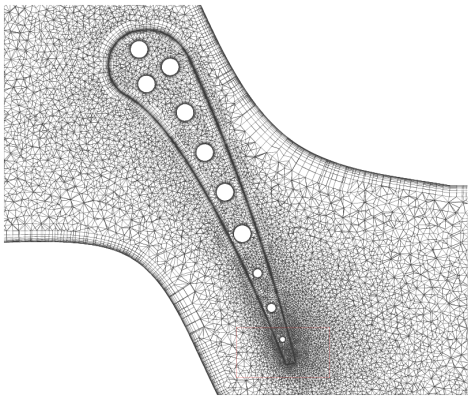

Figure 5.10 Computational grid on cross-sectional plane at the vane midspan

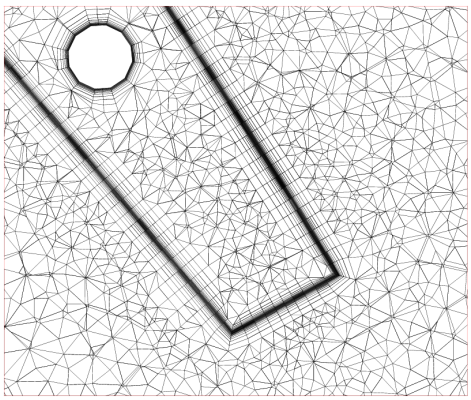

Figure 5.11 Zoomed view of the computational grid at the trailing edge

exhibit excellent agreement with the data of Hylton et al. [16]. On the suction side, the pressure falls very rapidly from the stagnation point, reaching a minimum value at $x\ C_x = 0\ 45$, where a shock occurs. Then the f ow is decelerated into subsonic range afterwards. The contour of Mach number on the midspan plane is given in Figure 5.13. The f ow shows strong acceleration along the suction side near the leading edge. The maximun Mach number is about 1.40 and drops after the shock.

The conjugate capability of the code is assessed using temperature and heat transfer predictions in both f uid f eld and metal blade region. Figure 5.14 shows predicted temperature contours at the midspan cutting plane. In the f uid f eld, a strong temperature gradient is observed near the shock and on the vane surface. On the blade, the temperature distribution is relatively smooth and is maintained at a low level, except near the trailing edge of the blade where the temperature becomes closer to the outside surface as the metal thickness decrease. Predicted surface temperature distributions at the blade midspan are

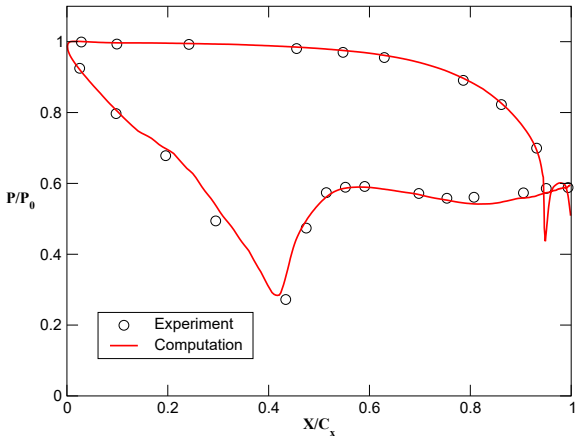


Figure 5.12 Predicted and measured pressure distribution curves for Case 1

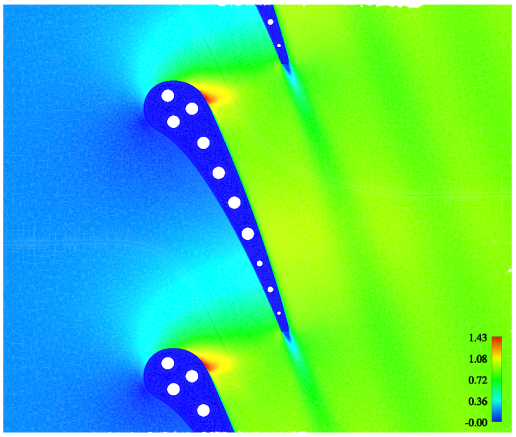


Figure 5.13 Predicted shaded contour plot of Mach number for Case 1

plotted with the experimental data in Figure 5.15. The result shows a very good agreement with the experiment; and all trends in temperature variations are matched by the computation. The average temperature is approximatly $0\ 56$, and the prediction of temperature is within $5\%$ of the experimental data over the entire airfoil. A local maximum temperature is observed in the vicinity of the stagnation point. Further downstream on both sides of the vane, the temperature increases wavily, as the trailing edge is approached. The temperature decreases where internal cooling channel becomes closer to the external airfoil surface. On the suction surface, the appearance of shock leads to a sharp increase in temperature.

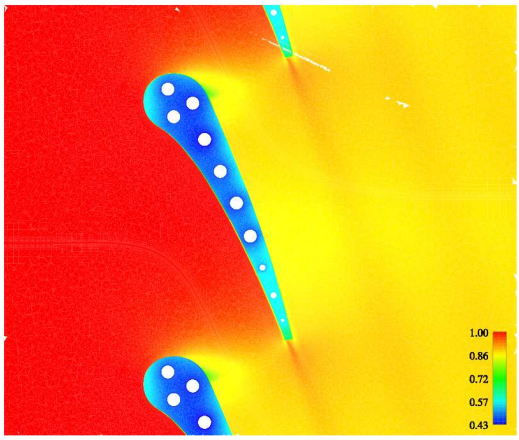


Figure 5.14 Predicted shaded contour plot of temperature for Case $1$

Heat transfer results are presented in terms of heat transfer coeff cient ($H$) on the external vane surface. Heat transfer coeff cient is derived from the surface normal temperature

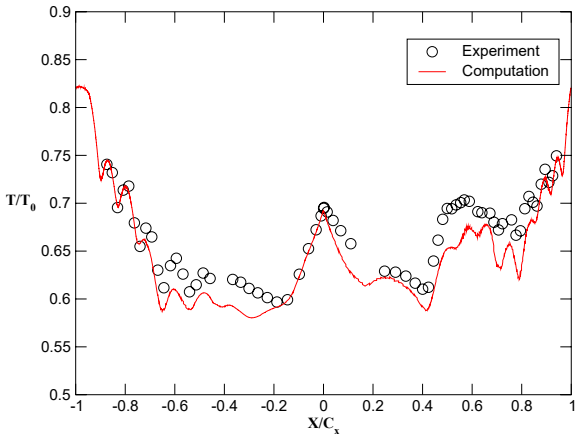


Figure 5.15 Predicted and measured temperature distribution curves for Case 1

gradient by equating the local normal conduction and the local convection [16]. $H$ is def ned by

$$H = \frac{q_w}{T_g \quad T_w} \tag{5.7}$$

Where $q_w$ is the vane surface heat f ux. $T_g$ and $T_w$ are the average gas temperature and the vane surface temperature respectively.

Numerical heat transfer coeff cient results are shown in Figure 5.16, along with the experimental data. General agreement is achieved on the whole prof le. There is a sharp decrease in the heat transfer coeff cient after the stagnation point on both suction and pressure surfaces, and the heat transfer coeff cient reaches maximum value after shock on the suction side. The suction surface heat transfer coeff cient distributions indicate boundary layer seperation and re-attachment starting at about $X \ C_x = 0\ 45$. Comparison

between Figure 5.16 and Figure 5.12 shows a clear correlation between the location of the separation and the strong adverse pressure distribution.

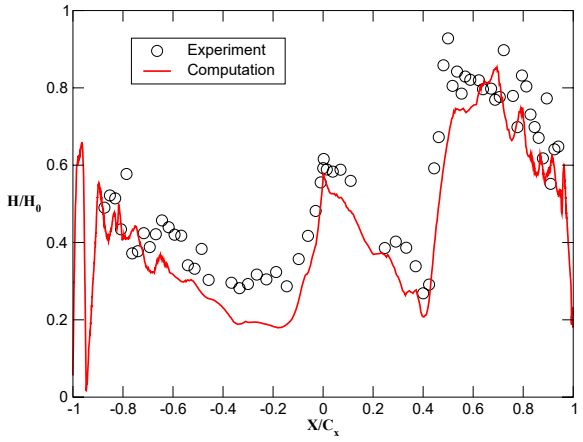


Figure 5.16 Predicted and measured heat transfer coeff cient distribution curves at the vane midspan plane for Case 1

Supersonic Case:

The predicted aerodynamic loading for Case 2 in the form of pressure distribution at the vane midspan is given in Figure 5.18, along with the experimental data. The predictions exhibit excellent agreement with the data of Hylton et al. [16]. On the suction side, the pressure falls very rapidly from the stagnation point, reaching a minimum value at $x \;\; C_x = 0\ 45$, where a shock occurs. Then the f ow is decelerated into subsonic range. Further downstream, the f ow is accelarated again before a second, weaker shock appears near the trailing edge. Contours of Mach number on the midspan plane is given in Figure 5.17.

The f ow shows strong acceleration along the suction side near the leading edge. The Mach number reaches maximum value of about 1.40 and drops after the shock.

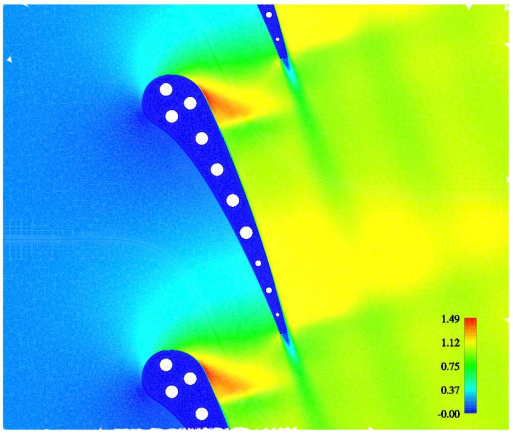


Figure 5.17 Predicted shaded contour plot of Mach number at the vane midspan plane for Case 2

With the aerodynamics validated, the heat transfer is investigated. The distribution of the dimensionless temperature on the vane external surface at the midspan is plotted in Figure 5.20, along with experimental data. Contours of temperature on the midspan plane is shown in Figure 5.19. A local maximum temperature can be observed in the vicinity of the stagnation point. Further on both sides of the vane, the temperature increases wavily, as the trailing edge is approached. A local maximum always exists between two cooling holes, and a local minimum is in the proximity of a hole, due to the low temperature of the coolant. On the suction side the shock leads to a sharp increase in temperature. The results show good agreement with the experimental results.

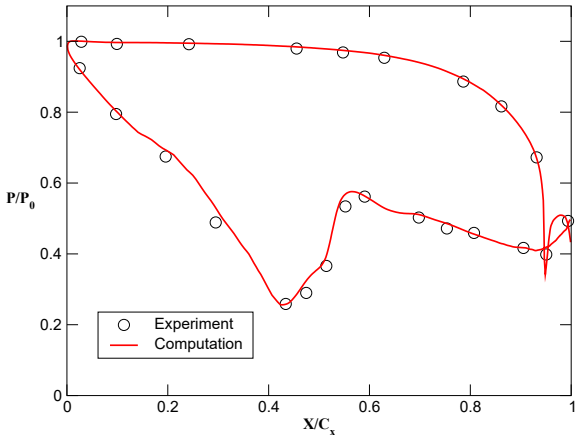


Figure 5.18 Predicted and measured pressure distribution curves for Case 2

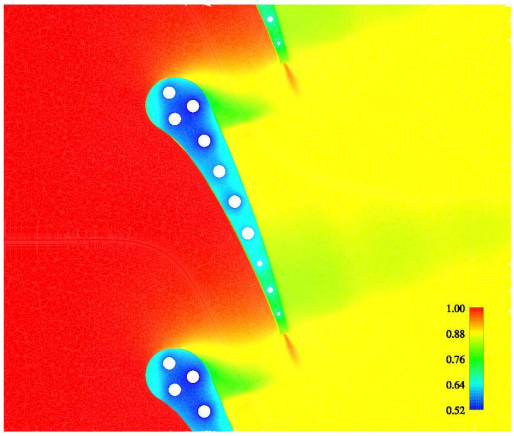


Figure 5.19 Predicted shaded contour plot of temperature at the vane midspan plane for Case 2

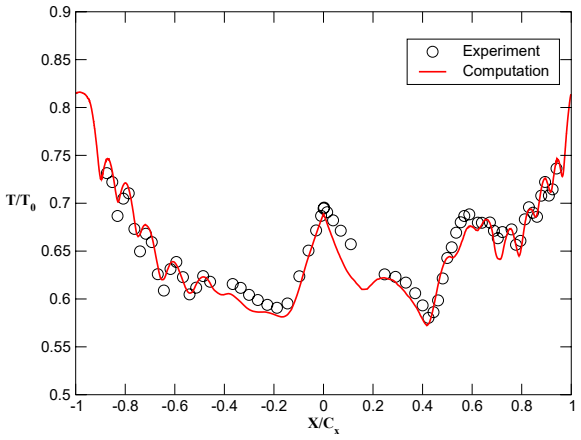


Figure 5.20 Predicted and measured temperature distribution curves for Case 2

Numerical heat transfer coeff cient results are shown in Figure 5.21, along with the experimental data. General agreement is achieved on the whole prof le. There is a sharp decrease in the heat transfer coeff cient after the stagnation point on both suction and pressure surfaces, and the heat transfer coeff cient reaches maximum value after shock on the suction side.

The computed aerodynamic loading and heat transfer using Spalart-Allaras models were compared with the experimental data. The aerodynamic loading and temperature show very good agreement with the experiments, and the heat transfer coeff cient also captures all the trends of the wavily increases along the vane surface. Reasonable agreement is observed for both subsonic and supersonic cases. The correlations between the temperature and heat transfer coeff cient are observed.

Comparisons between Different Turbulence Models:

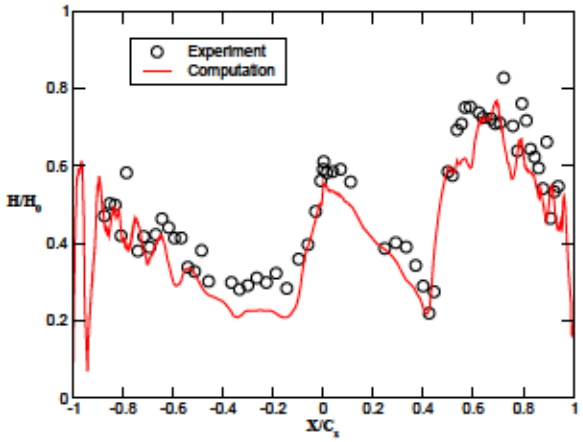


Figure 5.21 Predicted and measured heat transfer coeff cient distribution curves at the vane midspan plane for Case 2

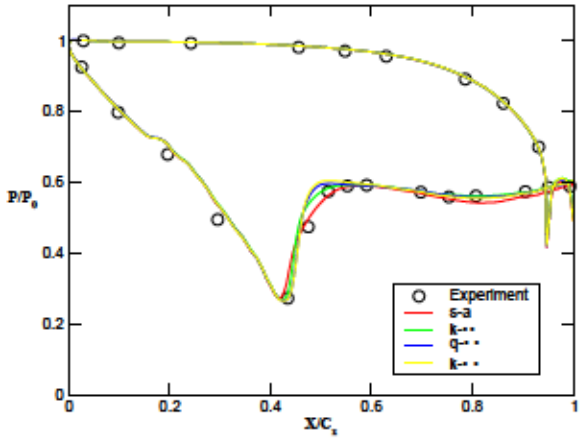


Figure 5.22 Comparison of predicted and measured pressure distributions between different turbulence models at the vane midspan plane for Case 1

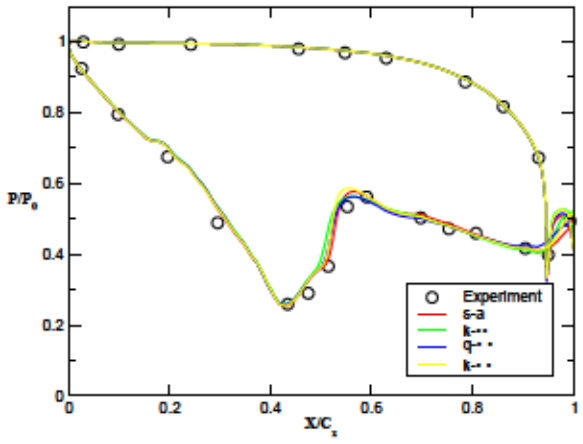


Figure 5.23 Comparison of predicted and measured pressure distributions between different turbulence models at the vane midspan plane for Case 2

Since the laminar-to-turbulent transition has impact on heat transfer behavior [26], three two-equation turbulence models were also used to asses the impact of transition on heat transfer behavior in the calculations. The static pressure, temperature, and heat transfer coeff cient were compared between different turbulence models.

For the aerodynamic loading data, the agreement between the experimental and all turbulence model results are quite well for both cases (Figure 5.22 and Figure 5.23), Although there is some difference between them in the vicinity of shock.

Predicted and experimental temperature prof les on the vane external surface at midspan for both cases are shown in Figure 5.24 and Figure 5.25. In addition, predicted and experimental heat transfer coeff cient prof les on the vane external surface at midspan for both cases are shown in Figure 5.26 and Figure 5.27. It is observed that the predicted temperatures and heat transfer coeff cients vary signif cantly among the different turbulence

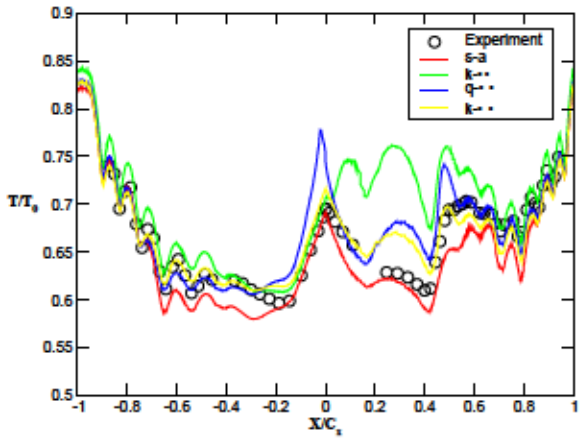


Figure 5.24 Comparison of predicted and measured temperature distributions between different turbulence models at the vane midspan plane for Case 1

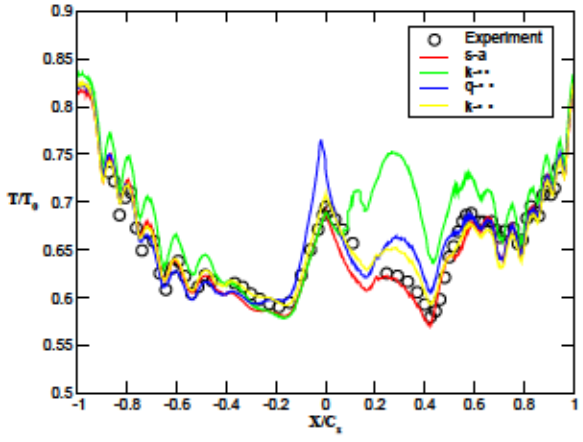


Figure 5.25 Comparison of predicted and measured temperature distributions between different turbulence models at the vane midspan plane for Case 2

models on the suction surface near the leading edge. It was reported in the experiment [16] that the large variations in the suction surface heat transfer coeff cients are caused by the seperation/re-attachment phenomena and transitional behavior. The onset and extent of the suction surface transitional behavior inf uences the heat transfer distribution. For the present cases, the boundary starts as a laminar f ow at the leading edge and transition to a turbulent boundary is expected to occur at some point downstream. All the two-equation turbulence models can not capture the transition, probably they force the boundary layer to be turbulent from the stagnation point and therefore numerical curves do not exhibit transitional behavior. This inability to predict an initial laminar boundary layer could be the main cause for the over prediction of the heat transfer coeff cient and temperatures.

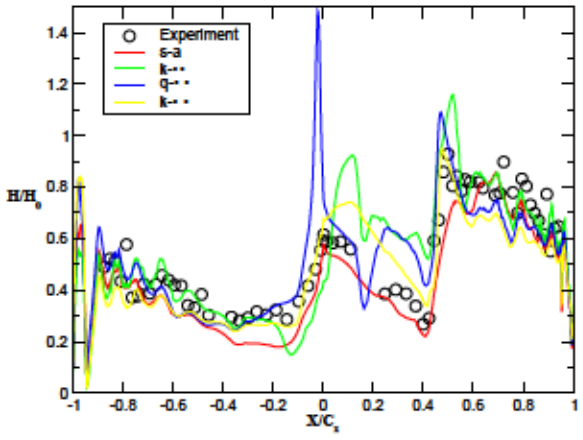


Figure 5.26 Heat transfer coeff cient distributions of different turbulence models for Case 1

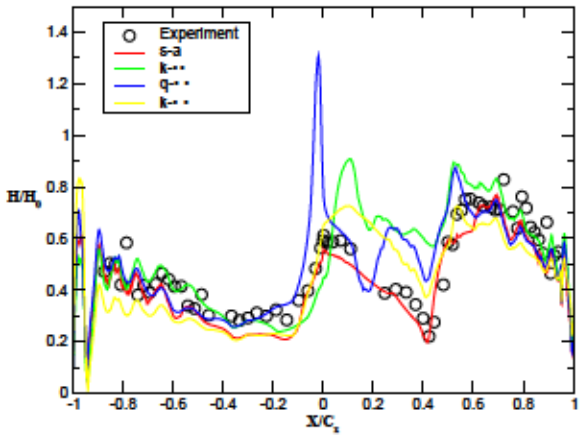


Figure 5.27 Heat transfer coeff cient distributions of different turbulence models for Case 2

### *5.2.3 Cooled Flat Plate*

This case is of multiple interfaces. It includes three parts: a solid plate, hot gas f owing on top of the plate, and coolant f owing from the bottom of the solid plate (Figure 5.28). The f ow is in the $x$ direction, and the $y$ direction is normal to the f at plate.

#### 5.2.3.1 Computational Grid and Boundary Conditions

The unstructured grid is shown in Figure 5.29. The grid consists of a total of $0.6$ million points. At both interfaces, $Y+ = 1$. The Spalart-Allmaras model was used for the computation. As the inlet conditions for the hot gas f ow, the Mach number is $0.2$, and a uniform temperature of $460K$ is specif ed. The coolant inlet temperature is $198K$. The solid plate conductivity is $k = 17.0W/mK$.

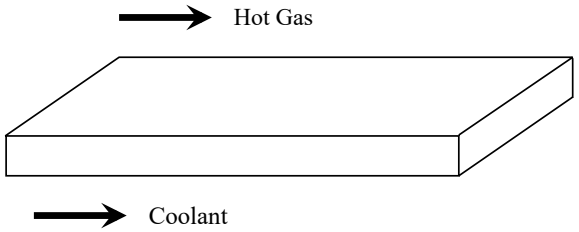


Figure 5.28 Schematic of the cooled f at plate

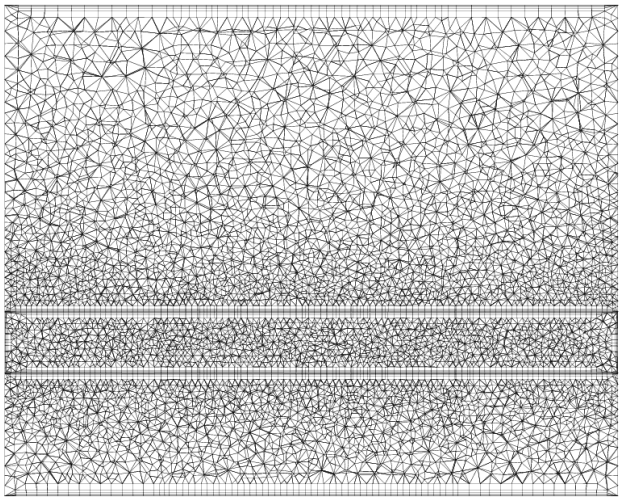

Figure 5.29 Computational grid for cooled f at plate

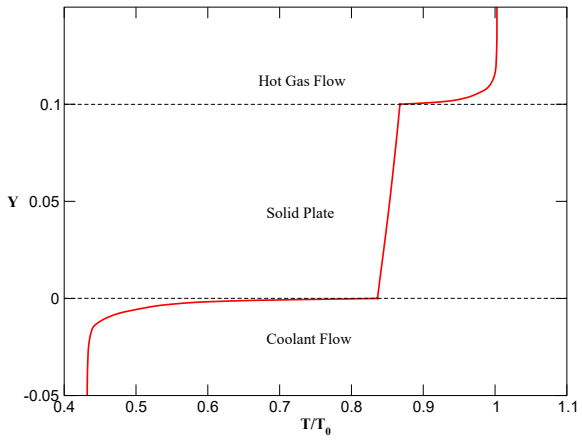


Figure 5.30 Temperature distribution in the normal direction ($y$) at $x = 0\ 5m$

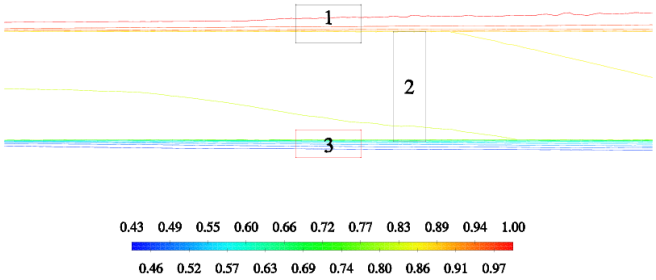


Figure 5.31 Temperature contour plot of the cooled f at plate at $z = 0$

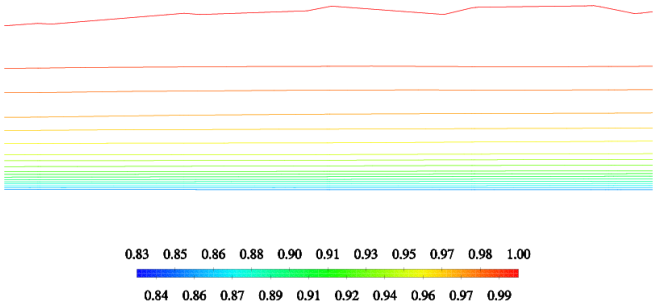


Figure 5.32 Temperature contour plot of the cooled f at plate at the location 1 (zoomed)

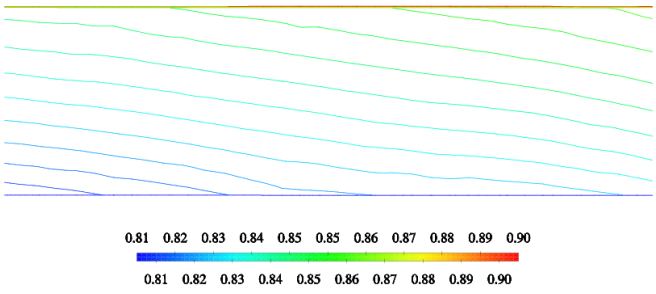


Figure 5.33 Temperature contour plot of the cooled f at plate at the location 2 (zoomed)

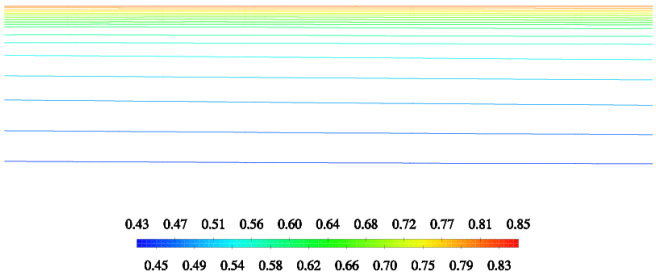


Figure 5.34 Temperature contour plot of the cooled f at plate at the location 3 (zoomed)

5.2.3.2 Results and Analysis

Figure 5.30 shows the dimensionless temperature prof le in the $y$ direction at $x = 0\ 5m$. One immediately can see from Figure 5.30 that the solid presents very little thermal resistance as evidenced by the small change in temperature in the solid. Temperature prof les in the hot gas and coolant exhibit the tubulent prof le. Figure 5.31 shows the temperature contours at a constant $z = 0$, and the hot gas f ow thermal boundary layer shows up as the tightly grouped contours on top of the f gure. The coolant f ow thermal boundary layer is shown by the tightly packed contours at the bottom. The relatively wide spaced contours represnt the temperature of the plate. Figure 5.32, Figure 5.33, and Figure 5.34 are the partly zoomed temperature contours at $z = 0$.

### *5.2.4 Effusion Cooled Plate*

As a representative test for the computational study of modern combustor liner heat transfer, an effusion-cooled plate is selected, which was experimentally and computationally investigated by Papanicolaou[2], Montomoli[13] and Martiny[27] etc..

#### 5.2.4.1 Geometry and Flow Conditions

The conf guration is shown in Figure 5.35. A f at plate with staggered rows of cylindrical holes, inclined at an angle of 17 degree in the f ow direction, is considered. The main supply of coolant comes from a plenum at the bottom, which is bounded vertically by adiabatic walls. The extremely small angle together with a small hole pitch provides a large area for convective cooling inside the holes.

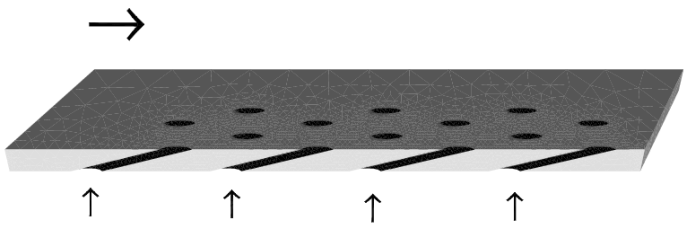

Figure 5.35 Schematic of Effusion Cooled Plate

The computational domain is illustrated in Figure 5.36. The plate is $12mm$ thick with an injection angle of $17$ degree. The holes have a staggered placement and a diameter of $5mm$. The thermal conductivity of the plate is $12\ 2W\ (mK)$. The unstructured grid of about $4\ 0$ million points is used, which includes the mainstream channel, plate and cooling holes.

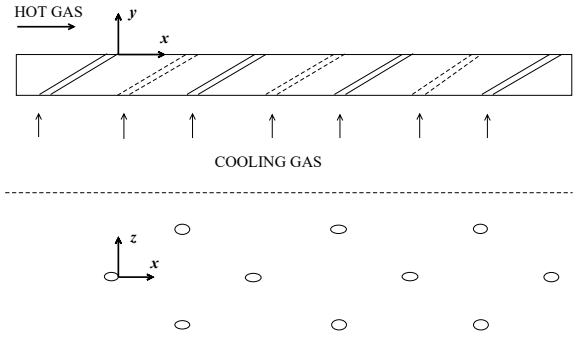


Figure 5.36 Computational Domain

As inlet conditions for the main gas f ow, the velocity of $28m\ s$ is specif ed. At the coolant inlet, vertical velocity is specif ed so that the desired blowing ratio ($M = {}_{c}u_{c} \quad {}_{m}u_{m}$) is obtained. The inlet temperature of the main f ow is of $550K$ uniformly. The coolant inlet temperature is set to $315K$. Here, there is some difference in the main f ow inlet condition between the simulation and experiment. The prof les of inlet temperature and velocity was used in experiment, however, constant values are specif ed in calculation.

5.2.4.2 Results and Discussion for blowing ratio of $M = 1\ 2$

Local temperature is plotted in Figure 5.37. The effect of the coverage of the previous injections is quite visible. The attached jet results in streaks of lower temperature. An increase is found aft of the rows of cooling holes, due to the the missing conductive inf uence of the f lm cooling holes.

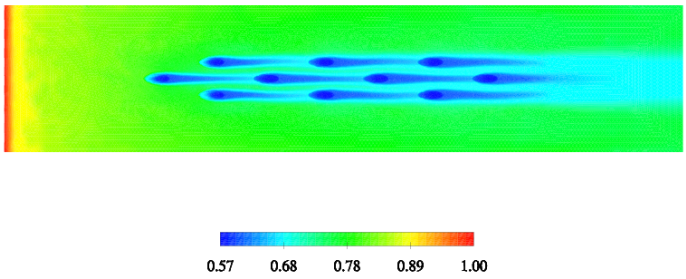


Figure 5.37 Predicted shaded contour plot of temperature at the plane of $y \ \ d = 0\ 01$

The heat transfer to the f lm-cooling plate is discussed in term of the normalized temperature ( ). It is def ned as

$$= \frac{T(y) \quad T_c}{T_0 \quad T_c} \tag{5.8}$$

$T_c$ is the temperature of the coolant at the inlet, and $T_0$ is the temperature at the inlet of hot gas channel.

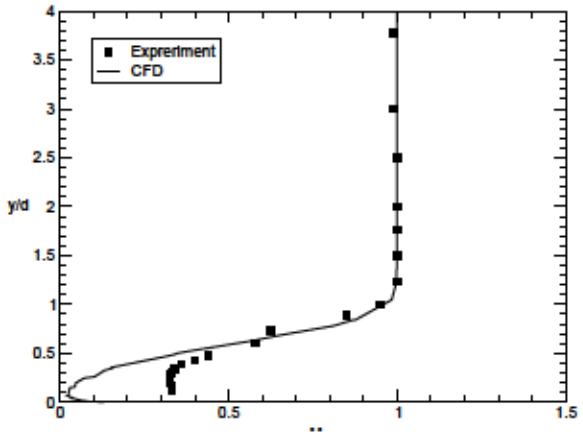


Figure 5.38 Computational and experimental temperature prof le at $x/d = 0.75$

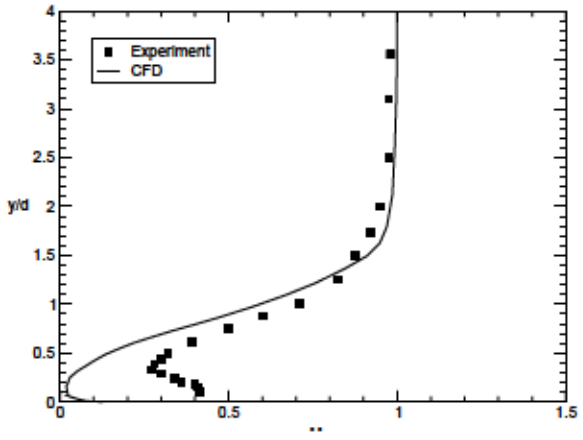


Figure 5.39 Computational and experimental temperature prof le at $x/d = 15.8$

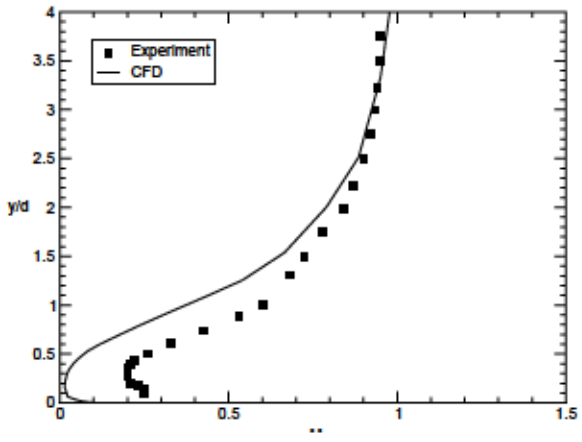


Figure 5.40 Computational and experimental temperature prof le at $x/d = 30.8$

The prof les of normalized temperature is investigated at the centerline location along the streamwise direction ($x$). As shown in Figure 5.38, Figure 5.39 and Figure 5.40, the temperature distributions are reported in comparison to the experimental data at three streamwise positions $x/d = 0.75$, $x/d = 15.8$ and $x/d = 30.8$ respectively (see Figure 5.36). $x/d = 0.75$ is located at downstream of the f rst holes row, $x/d = 15.8$ downstream the third row and $x/d = 30.8$ downstream the f fth row. Remarkable agreement between the calculation and experiment is found when $y/d$ is greater than $0.5$ at all three location, also the height of the thermal boundary layers are well predicted. For $y/d$ less than $0.5$, the predicted temperatures are lower than experimental data. As reported by the experiment, the coolant ejections f rst dettach the surface, and subsequently reattach it. There is penetration of hot gas f ow underneath the jets [27]. In the calculation, the coolant ejection attaches the surface (Figure 5.41) because the exact inlet boundary conditions from the experiment is not available, besides the effect of the inadquate specif cation

the thermal wall condition of the solid plate ([2], [13] and [28]). The attachments of ejections results in the lower temperature near the surface, as illustrated in the experiment by Gustafsson [29]. The calculation capatures the heat transfer phenomena of an effusion cooled plate. For this case, more work need to be done with exact boundary conditions in the future work.

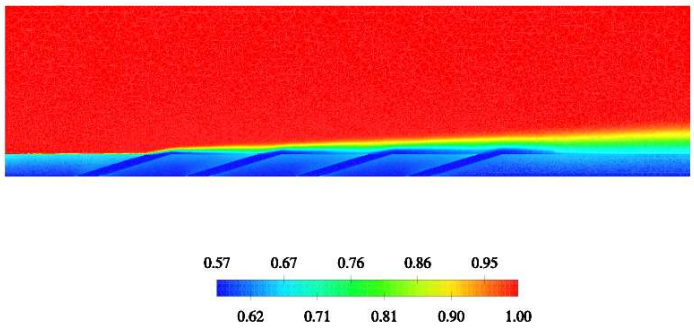


Figure 5.41 Computational temperature distribution at $z\ \ d = 0\ 0$

#### 5.2.4.3 Investigation for Three Blowing Ratios

Another two cases with blowing ratios of $M = 0\ 5$ and $M = 3\ 0$ have been computed. Also, the blowing ratio of $M = 1\ 2$ was calculated with an increase of the vertical velocity of the coolant. The streamwise velocity and temperature distributions are plotted with experimenatal data. All plots are at the centerline location along the streamwise di-

rection ($x$). $x/d = 0.75$ and $x/d = 0.75$ are located at downstream of the first holes row, $x/d = 15.8$ downstream the third row, $x/d = 30.8$ downstream the fifth row, $x/d = 45.8$ downstream the seventh row and $x/d = 60.7$ is located at the further down stream of the cooling holes.

The streamwise velocity profiles are plotted in Fig.5.42, Fig.5.43 and Fig.5.44 with some experimental data. It is obvious that the blowing ratio influence the streamwise velocity close to the wall surface. When the blowing ratio increases, the jet flow has a higher momentum resulting in a higher streamwise velocity.

The temperature profiles are also plotted (Fig.5.45, Fig.5.46 and Fig.5.47). The calculated temperature profiles show that they are not sensitive to the blow ratios. One possible reason is that at the downstream of the cooling holes, the jet flows are mixed with the main flow close to the wall surface even for the highest blowing ration ($M = 3.0$) due to the small angle of jet flow. This phenomena can be observed in the temperature contours in Fig. 5.51, Fig.5.52 and Fig.5.53.

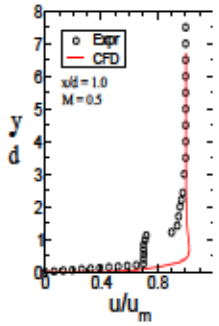


Figure 5.42 Computational streamwise velocity profiles for $M = 0.5$

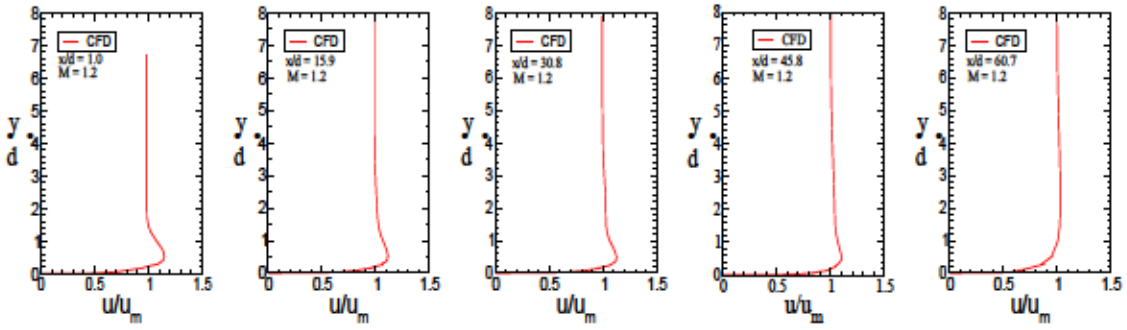


Figure 5.43 Computational streamwise velocity profiles for $M = 1.2$

The density (Fig. 5.48, Fig. 5.49 and Fig. 5.50) and temperature shaded contours (Fig. 5.51, Fig.5.52 and Fig.5.53) are plotted. The attachment and lift-off of jet can be observed. For the blowing ratio of $M = 3.0$, the density gradient shows the jet lift-off. Also, the temperature increases at the further downstream of the first row of cooling holes because of the detachment of the jet.

With the increase of blowing ratio ($M$), The attachment and lift-off of the coolant jet have been simulated. The resulting growing of the streamwise velocity near wall surface has been observed. It has been found that the cooling condition of $M = 3.0$ is worse than that of lower blowing ratios due to the jet lift-off. It is proved that the blowing ratio is a very important factor in the design of cooling scheme. The phenomena of effusion cooling have been captured in this work. Accuracy still need to be improved including the exact boundary condition, definition of the blowing ratio, and geometry.

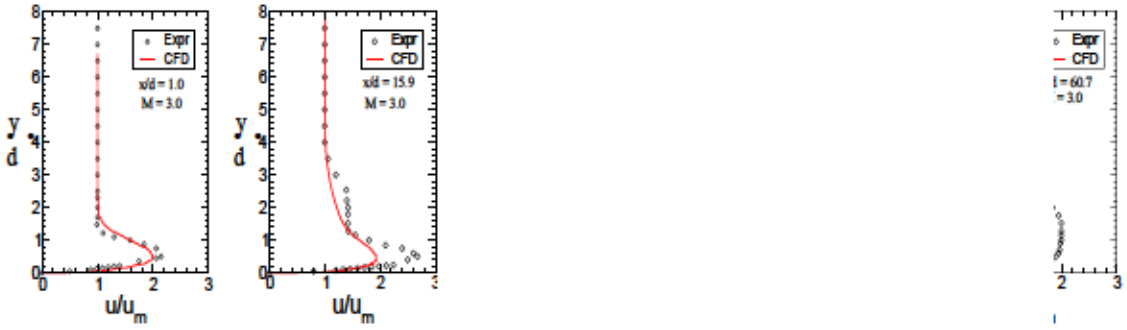


Figure 5.44 Computational streamwise velocity profiles for $M = 3.0$

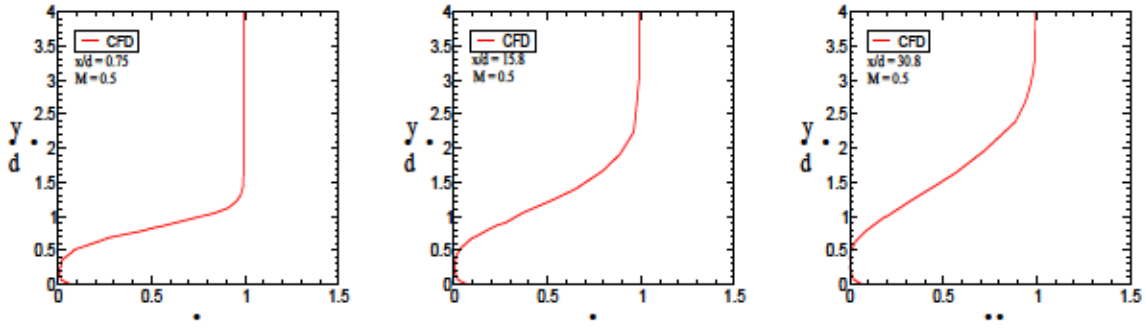


Figure 5.45 Computational temperature profiles for $M = 0.5$

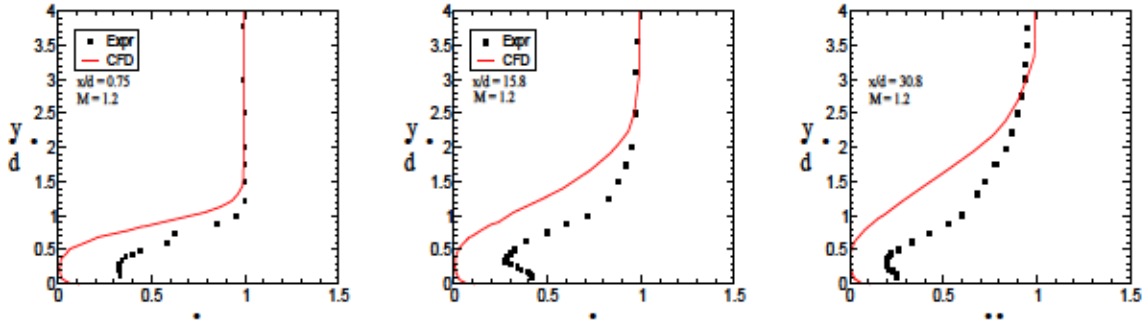


Figure 5.46 Computational temperature profiles for $M = 1.2$

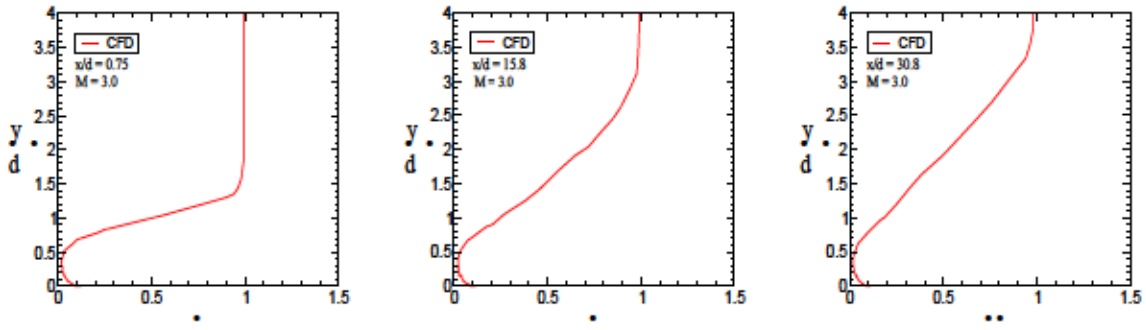


Figure 5.47 Computational temperature profiles for $M = 3.0$

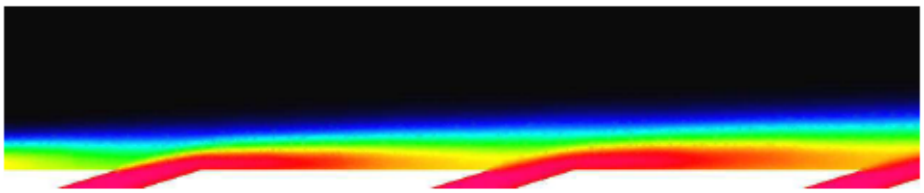

Figure 5.48 Computational shaded contour plot of density for $M = 0.5$

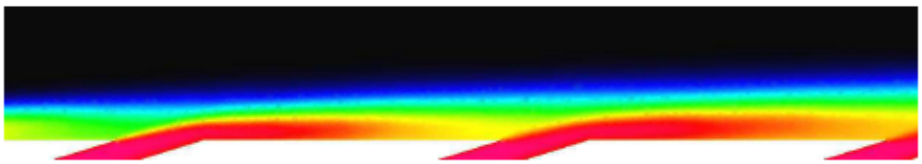

Figure 5.49 Computational shaded contour plot of density for $M = 1.2$

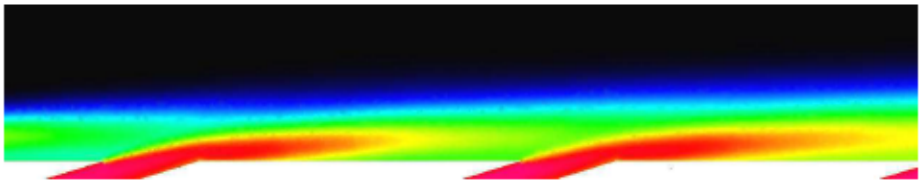

Figure 5.50 Computational shaded contour plot of density for $M = 3.0$

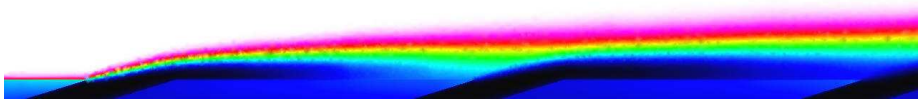

Figure 5.51 Computational shaded contour plot of temperature for $M = 0\ 5$

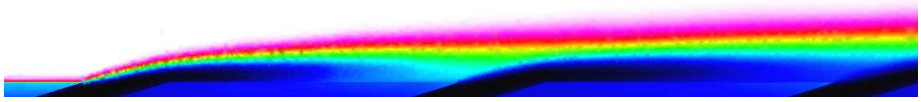

Figure 5.52 Computational shaded contour plot of temperature for $M = 1\ 2$

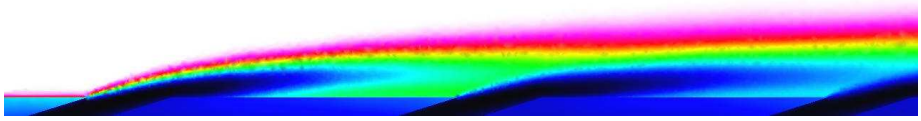

Figure 5.53 Computational shaded contour plot of temperature for $M = 3\ 0$

# CHAPTER VI

# SUMMARY AND CONCLUSIONS

The conjugate heat transfer solving capability has been successfully implemented in $U^2NCLE$ code using the fully-coupled approach and has been validated using several test cases. The method involves direct coupling of the internal flow, external flow, and heat conduction in the solid domain, and the same discretization and numerical methods are used for both fluid and solid domains calculations. The advantage of conjugate heat transfer is that heat transfer and temperature are the direct results of the calculation and any additional information, such as the heat transfer coefficient or temperature conditions, are not in need any more. Only the total pressure, total temperature and flow angles at inlets and the static pressure at flow outlets boundary conditions are necessary.

Test cases have been presented and validated with experimental data, including laminar and turbulent flows. In general, reasonable agreement between numerical calculations and both experimental data and analytical solutions and correlations are observed. For the flat plat flow and high pressure guide nozzle vane, the predicted aerodynamic loadings and temperatures show very good agreement with the analytical solution and experimental data. Reasonable agreement between predicted heat transfer coefficients and experimental data are observed, and all the trends are captured. The numerical code has also been

applied to an effusion-cooled plate, the positive effect of the f lm protection on the thermal load of the wall is obviously proved. The approach has demonstrated good accuracy and stability. The code will be a viable tool to predict the realitical thermal processes in the turbine blade and others.

It is also observed that turbulence model inf uences the heat transfer. One-equation and different two-equation models are used in the MarkII test cases. Aerodynamic loadings are found to be in good agreement with the experiments for all turbulence models. A little variation is shown in the position where the shocks occur on the suction surface in the leading edge for both cases. As evidenced by the measurements, the suction side exhibits a typical laminar to turbulence transitional behavior. For this reason and the current turbulence models do not include transition model which might fail to capture the transition processes in this region, so that the heat transfer coeff cient prof les obtained with the two equation turbulence models overpredicted the experimental data near the leading edge at the suction side. To use the benef ts of the conjugate approach, some improvements need to be carried out to predict the transional behavior.

# REFERENCES


[1] K. M. Kelkar, D. Choudhury, and M. Ambrosi, "Numerical Method for the Computation of Conjugate Heat Transfer in Nonorthogonal Boundary-Fitted Coordinates," *Numerical heat Transfer, Part B*, vol. 20, 1991, pp. 25–40.

[2] E. Papanicolaou, D. Giebert, R. Koch, and A. Schulz, "A Conservation-Based Discretization Approach for Conjugate Heat Transfer Calculations in Hot-Gas Ducting Turbomachinery Components," *International Journal of Heat and Mass Transfer*, vol. 44, 2001, pp. 3413–3429.

[3] J. D. Heidmann, A. J. Kassab, E. A. Divo, F. Rodriguez, and E. Steinthorsson, "Cojugate Heat Transfer Effects on A Realistic Film-Cooled Turbine Vane," *ASME Paper 03-GT-38553*, June 2003.

[4] D. L. Rigby and J. Lepicovsky, "Conjugate Heat Transfer Analysis of Internally Cooled Conf gurations," *ASME Paper 01-GT-0405*, June 2001.

[5] D. E. Bohn and C. Tummsers, "Numerical 3-D Conjugate Flow and Heat Transfer Invstigation of A Transonic Convection-Cooled Thermal Barrier Coated Turbine Guide Vane with Reduced Cooling Fluid Mass Flow," *ASME Paper 03-GT-38431*, June 2003.

[6] D. E. Bohn, J. Ren, and K. Kusterer, "Conjugate heat Transfer Analysis for Film Cooling Conf gurations with Different Hole Geomeries," *ASME Paper 03-GT-38369*, June 2003.

[7] K. Kusterer, D. E. Bohn, T. Sugimoto, and R. Tanaka, "Conjugate Calculations for A Film-Cooled Blade under Different Operating Conditions," *ASME Paper 04-GT-53719*, June 2004.

[8] W. D. York and J. H. Leylek, "Three-dimensional Conjugate Heat Transfer Simulation of An Internally-Cooled Gas Turbine Vane," *ASME Paper 03-GT-38551*, June 2003.

[9] B. Facchini, A. Magi, and A. S. D. Greco, "Conjugate Heat Transfer Simulation of A radially Cooled Gas Turbine Vane," *ASME Paper 04-GT-54213*, June 2004.

[10] J. R. Culham, S. Lee, and M. M. Yovanovich, "Conjugate Heat Transfer from a Raised Isothermal heat Source Attached to a Vertical Board," *Ninth IEEE SEMITHERM Symposium*, 1993.

[11] A. Horvat and I. Catton, "Numerical technique for Modeling Conjugate Heat Transfer in an Electronic Device Heat Sink," *International Journal of Heat and Mass Transfer*, vol. 46, 2003, pp. 2155–2168.

[12] Z. Han, B. H. Dennis, and G. S. Dulikravich, "Simultaneous Prediction if External Flow-Field and Temperature in Internally Cooled 3-D turbine Blade Material," *ASME Paper 00-GT-253*, May 2000.

[13] F. Montomoli, P. Adami, S. D. Gatta, and F. Martelli, "Conjugate Heat Transfer Modeling in Film Cooled Blades," *ASME Paper 04-GT-53177*, June 2004.

[14] R. S. Webster, *A Numerical Study of the Conjugate Conduv]ction-Convection Heat Transfer Problem*, doctoral dissertation, Mississippi State University, May 2001.

[15] Q. Liu, *Coupling Heat Transfer and Fluid Flow Solvers for Multi-Disciplinary Simulations*, doctoral dissertation, Mississippi State University, December 2003.

[16] L. D. Hylton, M. S, Mihelc, E. R. Turner, D. A. Nealy, and R. E. York, *Analytical and Experimental Evaluation of Heat Transfer Distribution Over the Surfaces of Turbine Vanes*, NASA Technical Report 168015, NASA Lewis Research Center, May 1983.

[17] C. Sheng, J. C. N. III, M. Remotigue, J. Chen, D. L. Marcum, and D. L. Whitf eld, *Development of Unstructured Computational Capabilities Applicable to MSU TURBO with an Arbitrary Mach Number Algorithm*, Tech. Rep. MSSU-COE-ERC-02-16, Mississippi State University, October 2002.

[18] D. G. Hyams, *An Investigation of Parallel Implicit Solution Algorithms for Incompressible Flows on Unstructured Topologies*, doctoral dissertation, Mississippi State University, May 2000.

[19] W. R. Briley, L. K. Taylor, and D. L. Whitf eld, "High-Resolution Viscous Flow Simulations at Arbitrary Mach Number," *Journal of Computational Physics*, vol. 184, 2003, pp. 79–105.

[20] D. L. Whitf eld and L. K. Taylor, "Discretized Newton-Relaxation Solution of High Resolution Flux-Difference Split Schemes," *AIAA Paper 91-1539*, June 1991.

[21] P. R. Spalart and S. R. Allmaras, "A One-Equation Turbulence Model for Aerodynamic Flows," *AIAA Paper 92-0439*, 1992.

[22] C. Sheng and Q. Xue, "Aerothermal analysis of turbine blades using an unstructured f ow solver - $U^2NCLE$," *AIAA paper 05-4683*, June 2005.

[23] C. Sheng and X. Wang, "Characteristic variable boundary conditions for arbitrary mach number algorithm in rotating frame," *AIAA paper 03-3976*, June 2003.

[24] F. J. Bayley, J. M. Owen, and A. B. Turner, *Heat Transfer*, Barnes and Noble Publishers, New York, 1972.

[25] A. V. Luikov, "Conjugate Convective Heat Transfer Problems," *International Journal of Heat Mass Transfer*, vol. 17, 1974, pp. 257–265.

[26] H. Schlichting, *Boundary Layer Theory*, McGram-Hill Book Company, New York, 1960.

[27] M. Martiny, R. Schiele, M. Gritsch, and A. S. andSoksik Kim, *High Intensity Combustor - Steady Isobaric Combustion: Final Report of the Collaborative Research Center 167*, chapter Heat Transfer and Radiation, WILEY, 2002, pp. 261–280.

[28] D. Giebert, E. Papanicolaou, C.-H. Rexroth, M. Scheuerlen, A. Schulz, and R. Koch, *High Intensity Combustor - Steady Isobaric Combustion: Final Report of the Collaborative Research Center 167*, chapter Heat Transfer and Radiation, WILEY, 2002, pp. 282–298.

[29] K. M. B. Gustafsson and T. G. Johansson, "An Experimental Study of Surface Temperature Distribution on Effusion-Cooled Plates," *Journal of Engineering for Gas Turbines and Power*, vol. 123, Jan 2001, pp. 308–316.